Effect of hydrodynamic slip on the rotational dynamics of a thin Brownian platelet in shear flow

Kamal, Catherine; Gravelle, Simon; Botto, Lorenzo

DOI
10.1017/jfm.2021.327

Publication date
2021

Document Version
Final published version

Published in
Journal of Fluid Mechanics

J. Fluid Mech. (2021), *vol*. 919, A1, doi:10.1017/jfm.2021.327

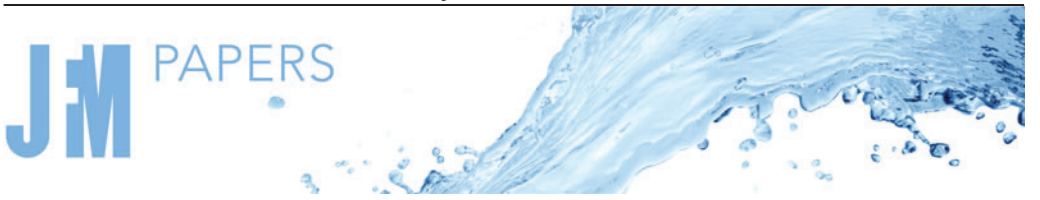

Effect of hydrodynamic slip on the rotational dynamics of a thin Brownian platelet in shear flow

Catherine Kamal[1], **Simon Gravelle**[1] **and Lorenzo Botto**[2],†

[1]School of Engineering and Material Science, Queen Mary University of London, London E1 4NS, United Kingdom

[2]Process and Energy Department, 3ME Faculty of Mechanical, Maritime and Materials Engineering, TU Delft, 2628 CD Delft, The Netherlands

(Received 28 February 2020; revised 26 January 2021; accepted 7 April 2021)

The classical theory by Jeffery predicts that, in the absence of Brownian fluctuations, a thin rigid platelet rotates continuously in a shear flow, performing periodic orbits. However, a stable orientation is possible if the surface of the platelet displays a hydrodynamic slip length λ comparable to or larger than the thickness of the platelet. In this article, by solving the Fokker–Plank equation for the orientation distribution function and corroborating the analysis with boundary integral simulations, we quantify a threshold Péclet number, Pe_c, above which such alignment occurs. We found that for Pe smaller than Pe_c, but larger than a second threshold, a regime emerges where Brownian fluctuations are strong enough to break the platelet's alignment and induce rotations, but with a period of rotation that depends on the value of λ. For Pe below this second threshold, slip has a negligible effect on the orientational dynamics. We use these thresholds to classify the dynamics of graphene-like nanoplatelets for realistic values of λ and apply our results to the quantification of the orientational contribution to the effective viscosity of a dilute suspension of nanoplatelets with slip. We find a non-monotonic variation of this term, with a minimum occurring when the slip length is comparable to the thickness of the particle.

Key words: suspensions, particle/fluid flow

1. Introduction

The flow behaviour of thin plate-like particles is of interest in many industrial and environmental applications, ranging from the processing of composite materials (Kumar, Sharma & Dixit 2019) to the transport of clay in natural waters (Tawari, Koch & Cohen 2001). Recently, the emergence of graphene and other two-dimensional (2-D)

† Email address for correspondence: l.botto@tudelft.nl

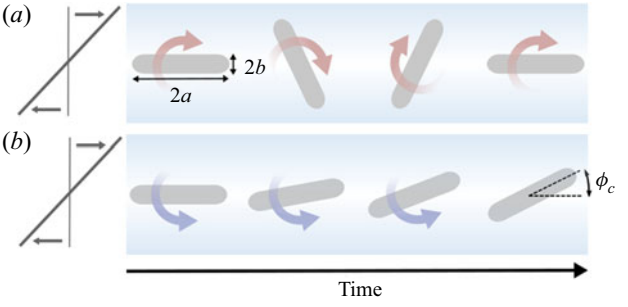

Figure 1. Sketch illustrating the rotational dynamics of a platelet having (*a*) zero slip length, as described by Jeffery's theory and (*b*) slip length λ significantly greater than the platelet's half-thickness b. The behaviours described in panels (*a*,*b*) are characteristic of the infinite Péclet number limit. In this paper we enquire about the effect of Brownian fluctuations on the rotational dynamics.

nanomaterials and their use in a variety of liquid-based processes (White *et al.* 2015; Del Giudice & Shen 2017; Koltonow *et al.* 2017; Karagiannidis *et al.* 2017) has spurred renewed interest in the dynamics of these extremely thin plate-like colloids when suspended in sheared liquids (Xu & Green 2014; Poulin *et al.* 2016; Reddy *et al.* 2018; Gravelle, Kamal & Botto 2021; Silmore, Strano & Swan 2021). In applications such as graphene inks or polymer nanocomposites, colloidal 2-D nanomaterials take the form of platelets of nanometric thickness and lateral size spanning from a few nanometres to a few microns (Wick *et al.* 2014). There is a great interest in understanding how the application of an external flow affects the orientation of these highly anisotropic particles in the presence of Brownian fluctuations. The surface of graphene and other 2-D nanomaterials can be characterised by a hydrodynamic slip length λ of several nanometres for many common solvents (Maali, Cohen-Bouhacina & Kellay 2008; Ortiz-Young *et al.* 2013; Tocci, Joly & Michaelides 2014), where λ is the distance within the solid at which the relative solid–fluid velocity extrapolates to zero (Bocquet & Barrat 2007); the mathematical definition of λ is given in § 4.3. For comparison, the typical thickness of 2-D material is < 1 nm. The aim of the current study is to understand the interplay between hydrodynamic slip and Brownian fluctuations in determining the rotational dynamics of a thin plate in an unbounded, simple shear flow under creeping flow conditions.

According to Jeffery's (1922) classical theory, derived for the high-Péclet number limit in which Brownian fluctuations are negligible, an oblate ellipsoid with its normal in the flow plane rotates continuously, performing a characteristic tumbling dynamics (figure 1*a*). Bretherton (1962) generalised the high-Péclet, low-Reynolds-numbers theory of Jeffery to axisymmetric particles of general shape. Bretherton's analysis showed that for axisymmetric shapes the rotational dynamics is governed by a scalar parameter that depends, for a no-slip particle, only on the shape of the particle. For instance, for an oblate ellipsoidal particle of major semiaxis a and minor semiaxis b, the scalar parameter identified by Bretherton corresponds simply to the geometric aspect ratio b/a. However, when hydrodynamic slip is present, Bretherton's scalar parameter (which we shall name k_e in the current article) is not only a function of b/a but must also depend on the slip length λ (Zhang, Xu & Qian 2015; Kamal, Gravelle & Botto 2020). This brings about the question of how slip affects Jeffery's predictions, and how Brownian fluctuations alter the rotational dynamics when the slip length is large in comparison with the particle thickness. This question is particularly relevant considering the nanometric thickness of 2-D nanomaterial particles.

Hydrodynamic slip at solid boundaries is known to affect the motion of small rigid particles in fluids. Slip reduces the tangential hydrodynamic stress on the particle surface (Sellier 2013), resulting in a reduction in the translational and rotational drag coefficient of spherical or anisotropic particles (Youngren & Acrivos 1975; Loyalka & Griffin 1994; Allison 1999; Keh & Huang 2004; Keh & Chang 2008; Sellier 2012; Chang & Keh 2012; Sherwood 2012). Slip also results in a slowdown of the rotational dynamics of spherical particles freely suspended in a simple shear flow (Luo & Pozrikidis 2008). A similar slip-dependent slowdown in a shear flow was predicted by Zhang *et al.* (2015) for a particle with an elliptic cross-section ($b/a \sim 0.5$) and infinite extent in the vorticity direction, in the limit of a slip length smaller than the particle thickness ($\lambda \sim b/5$).

Recently, we studied the motion of a thin ($b/a \ll 1$) rigid graphene-like nanoparticle with hydrodynamic slip (Kamal *et al.* 2020), via a combination of molecular dynamics (MD) and continuum simulations. In contrast to previous studies (Zhang *et al.* 2015), we considered values of the slip length either larger or smaller than the particle thickness. By using numerical and asymptotic solutions of the low-Reynolds-number boundary integral equations governing the hydrodynamic surface stress distribution, we showed that provided that the half-thickness of the platelet b is smaller than λ, in the limit of infinite Péclet (Pe) numbers the platelet aligns at a small angle ϕ_c with respect to the flow direction, instead of performing full rotational cycles as predicted by Jeffery's theory for $Pe \to \infty$ (figure 1*b*). Our asymptotic analysis revealed that this behaviour is due to a perturbed balance between two hydrodynamic torque contributions. One contribution is due to tangential hydrodynamic stresses acting on a lever arm proportional to b. The second contribution is due to normal hydrodynamic stresses acting on a lever arm proportional to a. For $\lambda/b \ll 1$ the torque due to tangential stresses is larger than that due to normal stresses, resulting in an expected rotation in the same direction of the vorticity vector (Singh *et al.* 2014). However, we demonstrated that to leading order in b/a slip induces a reduction in the tangential stresses, without affecting the normal stresses significantly. As a consequence, for $\lambda/b \gtrapprox 1$ the torque due to normal stresses dominates, resulting in a rotation in the direction opposite to the vorticity vector (for a particle initially aligned in the flow direction, as illustrated in figure 1*b*) and the attainment of an equilibrium angle ϕ_c in correspondence to which the two torque contributions balance exactly (an illustration of such arrested dynamics is given in § 4). This surprising result was confirmed with MD simulations. While the theory we developed was for infinite values of Pe for which the effect of Brownian fluctuations is negligible, we observed a stable orientation in MD simulations of relatively short graphene nanoplatelets for Pe of approximately 100 (Kamal *et al.* 2020). This raises the question of what is the minimum Pe for which a stable orientation can be observed.

In this paper we first recall the essential elements of the high-Pe number theory we developed previously. Then we analyse the rotational dynamics for finite Pe numbers, by considering solutions of the Fokker–Plank equation governing the single-particle orientational distribution function. To simplify the problem, following Leahy, Koch & Cohen (2015) we assume that the motion of the particle is in the flow plane, hence the orientational distribution is a function only of the angle with respect to the flow direction and time. Earliest work on the use of the Fokker–Plank equation for predicting the orientational distribution of elongated particles in a shear flow is due to Burgers (1938) and Peterlin (1938), who examined the effects of Brownian fluctuations on the dynamics of ellipsoids and rods for $Pe \ll 1$. Other authors have examined the range $Pe \gg 1$ (Leal & Hinch 1971; Hinch & Leal 1973; Leahy *et al.* 2015) and the range of intermediate Pe (Sadron 1953; Scheraga 1955; Hinch & Leal 1972; Férec *et al.* 2008), considering ellipsoids (both oblate and prolate) and more general rod-like particles. An important

result of these theoretical and numerical analyses is that for elongated particles almost aligned with the flow, Brownian fluctuations increase the average particle's rate of rotation with respect to the high-*Pe* value, essentially by allowing the particle to escape from the region of small streamwise velocity. Theories for the rotational dynamics of elongated particles based on the seminal work of Jeffery have been confirmed experimentally for a range of *Pe* numbers by standard rheological measurements (Ivanov, Van de Ven & Mason 1982; Mueller, Llewellin & Mader 2009), rheo-optics (Frattini & Fuller 1986; Fuller 1995; Vermant, Yang & Fuller 2001; Reddy *et al.* 2011) and by direct observation of the dynamics of single particles (Anczurowski & Mason 1967*b*; Stover, Koch & Cohen 1992; Herzhaft & Guazzelli 1999; Leahy *et al.* 2013). We are not aware of experimental work on the rotational dynamics of plate-like particles specifically focusing on the effect of slip.

The structure of the paper is as follows. In § 2 we analyse Bretheton's equation of motion. We show that this equation can be used to describe the rotational dynamics of plate-like particles with slip, provided that when λ/b is larger than a threshold value the effective aspect ratio of the particle is taken to be a complex number. In § 3, we consider numerical solutions of the Fokker–Plank equations for the orientational distribution function. The objective of this section is to illustrate the qualitative features of the particle dynamics and quantify the range of *Pe* above which the effect of slip-dependent hydrodynamics becomes important. Such analysis enabled us to estimate the threshold *Pe* giving a stable orientation. In § 4, we apply our theory to the dynamics of nanoplatelets whose geometry mimics that of single and multilayer graphene, for practically relevant values of λ. In this section, we quantify the threshold shear stress needed to prevent the platelet from completing full rotations. Finally, we analyse how the indefinite alignment of the particles affects the orientational contribution to the effective viscosity of a diluted suspension of platelets with slip.

2. Formulation of the problem

We consider the rotational dynamics of a rigid plate-like particle (henceforth referred to as 'platelet') in a simple shear flow. The platelet has length $2a$ and thickness $2b$. We work under conditions of Stokes flow and neglect particle inertia and gravity (i.e., the particle is force and torque free). In our theoretical derivations, we assume that the geometric aspect ratio $k = b/a$ is much smaller than one. A consequence of this is that the rotational dynamics of a three-dimensional (3-D) platelet can be well approximated by the rotational dynamics of a 2-D platelet of infinite extent in the vorticity direction, provided that the motion of the particle occurs in the plane of the flow and the depth of the platelet's extent in the vorticity direction is not small in comparison with its length (Kamal *et al.* 2020). We assume that the particle is symmetric about two planes (lines in two dimensions) passing through the particle centre. The particle motion is induced by an undisturbed shear flow field $\boldsymbol{u}_\infty = \dot{\gamma} y \hat{\boldsymbol{e}}_x$, where $\hat{\boldsymbol{e}}_x$ is the unit normal in the flow direction and $\dot{\gamma}$ is the shear rate.

The probability p of finding the platelet at a certain angle with respect to the flow, in response to both hydrodynamic and Brownian stresses, is governed by a Fokker–Planck (Smoluchowski) equation (Gardiner 2004). With just one degree of freedom, the Fokker–Planck equation for the orientational probability distribution function simplifies to a second-order partial differential equation,

$$\dot{p} = \left[D_r p_\phi - \dot{\gamma}\, \Omega p \right]_\phi , \tag{2.1}$$

where ϕ is the anticlockwise orientation angle with respect to $\hat{\boldsymbol{e}}_x$, t is time, $\dot{p} = \partial p/\partial t$, $[\,]_\phi = \partial[\,]/\partial\phi$, $\Omega(\phi)$ is the hydrodynamic angular velocity non-dimensionalised by $\dot{\gamma}^{-1}$

and D_r is the rotational diffusion coefficient. The ratio of convective and diffusive fluxes in (2.1) is the Péclet number $Pe = \dot{\gamma}/D_r$.

2.1. *Hydrodynamic angular velocity*

The hydrodynamic angular velocity $\dot{\gamma}\Omega$ is required to close (2.1). In the dilute limit, Ω can be evaluated by examining the motion of an isolated freely suspended platelet in the absence of Brownian fluctuations. For a symmetric platelet, Ω can be calculated exactly by using Bretherton's (1962) equation of motion (Kim & Karrila 2013). This equation describes the relationship between the time derivatives of the particle orientation vector $\boldsymbol{d}$, and the rate of strain and vorticity tensors associated with the undisturbed flow field, $\boldsymbol{\Omega}_\infty = (\boldsymbol{\nabla u}_\infty + \boldsymbol{\nabla u}_\infty^T)$ and $\boldsymbol{E}_\infty = (\boldsymbol{\nabla u}_\infty - \boldsymbol{\nabla u}_\infty^T)$, respectively, as follows:

$$\dot{\boldsymbol{d}} = \dot{\gamma}\boldsymbol{\Omega} \times \boldsymbol{d} = \boldsymbol{\Omega}_\infty \times \boldsymbol{d} + \left(\frac{k_e^2 - 1}{k_e^2 + 1}\right)(\boldsymbol{E}_\infty \cdot \boldsymbol{d} - \boldsymbol{E}_\infty \boldsymbol{dd}\,\boldsymbol{d}). \tag{2.2}$$

Using spherical polar coordinates, the orientation vector can be expressed as $\boldsymbol{d} = \sin\theta\cos\phi\hat{\boldsymbol{e}}_x + \sin\theta\sin\phi\hat{\boldsymbol{e}}_y + \cos\theta\hat{\boldsymbol{e}}_z$, resulting in the following coupled ordinary differential equations (Kim & Karrila 2013):

$$\dot{\theta} = \left(\frac{1 - k_e^2}{1 + k_e^2}\right)\frac{\dot{\gamma}}{4}\sin 2\theta \sin 2\phi, \quad \dot{\phi} \equiv \dot{\gamma}\Omega = -\frac{\dot{\gamma}}{k_e^2 + 1}\left(k_e^2\cos^2\phi + \sin^2\phi\right). \tag{2.3}$$

Note that $\dot{\phi}$ does not depend on θ, hence an analysis of the particular 2-D case considered here corresponding to $\theta = \pi/2$ is representative of the ϕ-dependence for all values of θ. The derivation of Bretherton's equation of motion does not make assumptions regarding the boundary condition at the solid surface and therefore applies to platelets with slip. This equation depends on the value of k_e, which in turn depends on the slip length as well as on the platelet's shape (Luo & Pozrikidis 2008; Kamal *et al.* 2020). The parameter k_e can be calculated for $\theta = \pi/2$ as the ratio between the hydrodynamic torques acting on a particle held fixed with its long axis held parallel to the flow, $T(0)$, or perpendicular to the flow, $T(\pi/2)$, according to the following expression (Cox 1971):

$$k_e = \sqrt{\frac{T(0)}{T(\pi/2)}}. \tag{2.4}$$

For a platelet satisfying the no-slip boundary condition, $T(0)/T(\pi/2)$ is positive and therefore k_e is a real number (Willis 1977). In this case, when the geometric aspect ratio $k = b/a \ll 1$, the parameter k_e follows a power-law relationship $k_e \propto k^n$ where n is an exponent that depends on the specific geometry of the platelet. For this reason, k_e is often called the 'effective aspect ratio'. For example, an ellipsoid with a no-slip surface has $k_e = k$ (Jeffery 1922), and a disk with blunt edges has $k_e \propto k^{3/4}$ (Singh *et al.* 2014). For real k_e the solution to (2.3) is

$$\tan\theta = \frac{Ck_e}{\sqrt{k_e^2\cos^2\phi + \sin^2\phi}}, \quad \tan\phi = -k_e\tan\left(\frac{\dot{\gamma}t}{k_e + k_e^{-1}}\right), \tag{2.5a,b}$$

where C is a positive integration constant. These equations describe periodic rotations of the particle called 'Jeffery orbits'; the time period of such rotations is

$$P = 2\pi\dot{\gamma}^{-1}(k_e + k_e^{-1}). \tag{2.6}$$

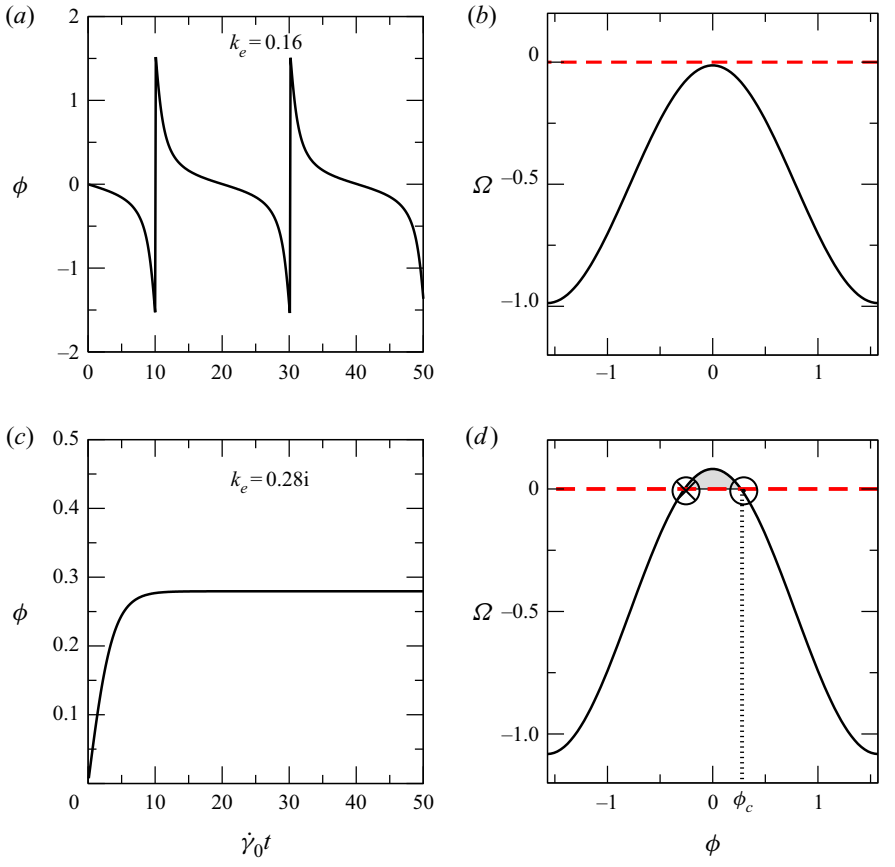

Figure 2. (*a*) Rotation angle ϕ for a particle with real effective aspect ratio $k_e = 0.16$ and $Pe = \infty$. (*b*) Associated angular velocity $\dot{\gamma}\Omega$; notice that $\Omega < 0\ \forall\phi$. (*c*) Rotation angle ϕ for a particle with imaginary effective aspect ratio $k_e = 0.28\mathrm{i}$ and $Pe = \infty$, showing stabilisation at $\phi_c \approx 0.27$. (*d*) Corresponding non-dimensional angular velocity, with the two equilibrium points at $\phi = \pm\phi_c$. The '$\odot$' symbol marks the stable angle ϕ_c; the angle denoted by '$\otimes$' is unstable.

The value of C depends on $\theta(0)$; for $\theta(0) = \pi/2$, $C \to \infty$ and $\theta(t) = \pi/2$ for all values of t. Thus, a particle initially rotating in the plane of the flow will continue rotating in the plane of the flow. This is the situation we are aiming to model in the current paper. For finite Pe numbers, trajectories out of the $\theta = \pi/2$ plane are of course possible. The case $\theta = \pi/2$ for finite Pe is tractable analytically and has been shown, in the no-slip case, to be relevant to the full 3-D dynamics (Leahy *et al.* 2015). In § 3 we shall consider the general slip case at finite Pe.

An example of an orbit for $\theta = \pi/2$ and real k_e and the corresponding $\Omega(\phi)$ are given in figures 2(*a*) and 2(*b*), respectively. Since $k_e \ll 1$, the time scale for the particle to flip is much smaller than the time spent by the particle near $\phi = 0$ (Singh *et al.* 2014). For a no-slip platelet of vanishing thickness, $k_e \to 0$ as $k \to 0$ and thus the particle will remain in a fixed position in the *ad hoc* case $k = 0$ (Bretherton 1962). Otherwise the platelet will rotate (unless the platelet has a specially designed, slightly non-axisymmetric shape, see Borker, Stroock & Koch (2018)).

For platelets presenting a surface with slip, however, such alignment is possible (Kamal *et al.* 2020). The effect of surface slip is to reduce the value of k_e^2, such that the $\Omega(\phi)$

curve shifts upwards, reducing the frequency of rotation with respect to the no-slip case (Luo & Pozrikidis 2008; Zhang *et al.* 2015; Kamal *et al.* 2020). At or above a critical slip length that scales with the thickness of the platelet, k_e^2 becomes negative, and so $\Omega(\phi)$ will be shifted onto or above the zero line (figure 2*d*). Such a solution corresponds to a negative value of $T(0)/T(\pi/2)$ and a purely imaginary complex value of k_e (Kamal *et al.* 2020). It is instructive to compare the structure of the $\phi - \theta$ equations (describing full 3-D trajectories) for pure and imaginary values of k_e. For a purely imaginary k_e, the solution of (2.3) is

$$\tan\theta = \frac{C|k_e|}{|k_e|^2\cos^2\phi + \sin^2\phi}, \quad \tan\phi = |k_e|\tanh\left(\frac{\dot{\gamma}t}{|k_e|^{-1} - |k_e|}\right). \tag{2.7a,b}$$

Comparing with (2.5*a*,*b*), whilst the equation for θ remains unchanged with respect to the case of a real k_e, the equation for ϕ now admits a stable non-periodic solution for $t \to \infty$. The particle relaxes to the stable orientation angle $\phi_c = \arctan(|k_e|)$, as shown in figure 2(*c*). For this angle, Ω has a positive zero root, indicated by the open circle in figure 2(*d*). The relaxation to equilibrium occurs on a time scale

$$P_R = \dot{\gamma}^{-1}(|k_e|^{-1} - |k_e|), \tag{2.8}$$

to be compared with the rotational time period of (2.6). For $|k_e| \ll 1$, P and P_R are proportional to each other. We note that a stable orientation has been predicted for blood cells in shear flow in the case of small internal-to-external viscosity ratios (due to the so-called 'tank-treading' motion, see e.g. Keller & Skalak (1982)). The analogy with our case is, however, only qualitative, because there is no single slip parameter that can model the dynamic coupling between inner and outer fluids seen in blood cells.

Surface slip at infinite Péclet number thus has significant effects on the rotational dynamics of a platelet. When the slip length is smaller than the platelet's thickness, slip reduces the frequency of the rotational orbits through a decrease in the value of k_e. However, when the slip length is greater than a threshold value comparable to the platelet's thickness, the platelet aligns indefinitely at an angle ϕ_c with the flow.

3. Rotational dynamics at finite Péclet numbers

At finite *Pe*, both the rotational diffusion coefficient D_r and the effective aspect ratio k_e change due to slip. However, in the limit $k \to 0$, D_r becomes approximately independent of λ (Sherwood & Meeten 1991; Sherwood 2012). Therefore, for thin platelets, the rotational dynamics at finite *Pe* changes primarily due to slip through the dependence of k_e on the hydrodynamic angular velocity.

3.1. *Random walk trajectories*

To illustrate the effects of Brownian fluctuations on the platelet's rotational trajectories, we solve numerically the Langevin representation of (2.1) for different *Pe* and k_e. In finite difference form, such Langevin representation describes simply connected paths in the particle orientational space. Using a first-order approximation of the time derivative, the resulting stochastic finite difference equation is (Doi & Edwards 1988)

$$\Delta\phi = \dot{\gamma}\Omega(\phi)\Delta t + X. \tag{3.1}$$

Here, we take X as a Gaussian random variable with zero mean and variance $\langle X^2\rangle = 2D_r\Delta t$. Solving numerically this equation for several sequences of random numbers

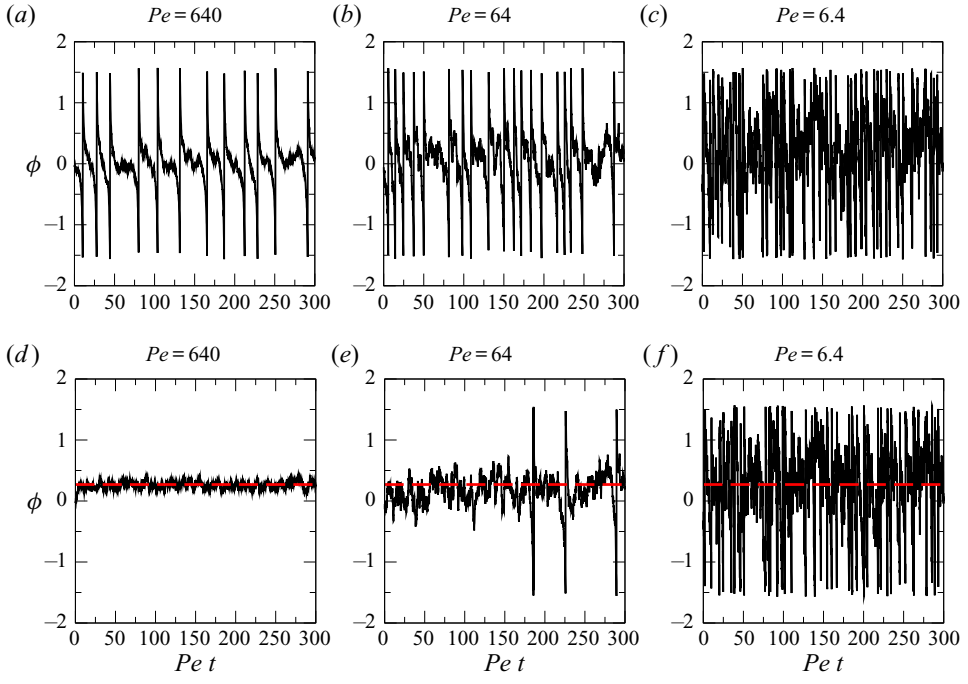

Figure 3. Time evolution of the rotation angle for different Pe, as calculated from (3.1), comparing (a–c) real k_e ($k_e = 0.11$) to (d–f) purely imaginary k_e ($k_e = 0.21\mathrm{i}$). The red dashed line is the value of ϕ_c obtained for $Pe \to \infty$.

provides a set of trajectories distributed according to (2.1). Examples of trajectories calculated from (3.1) for different Pe are shown in figure 3, comparing the cases of real and purely imaginary k_e. Full rotational cycles, corresponding to a platelet travelling through the full range $\phi \in [-\pi/2, \pi/2]$, can always be observed if k_e is real. When k_e is real, the average time period (in units of Pe t) for the platelet to perform a full rotational cycle decreases as Pe decreases (figure 3a–c). This behaviour has been predicted in previous theoretical studies on the steady-state rotatory dynamics of plate-like particles (Leal & Hinch 1971; Hinch & Leal 1972), and is in agreement with experiments where the instantaneous rotations of elongated particles have been visualised directly (Stover *et al.* 1992; Herzhaft & Guazzelli 1999; Leahy *et al.* 2013), or through rheo-optical or neutron diffraction techniques (Frattini & Fuller 1986; Jogun & Zukoski 1999; Brown *et al.* 2000). In contrast, if k_e is purely imaginary, for large Pe ($Pe = 640$), the platelet fluctuates around a stable orientation angle (figure 3d–f). This angle is approximately the same as the equilibrium angle for $Pe \to \infty$ ($\phi_c = \arctan|k_e|$). When Pe decreases below a threshold value, Brownian fluctuations cause the platelet to perform full rotational cycles. However, the average frequency of these full rotational cycles is significantly reduced in comparison with the no slip case, as seen by the reduction of the number of peaks in figure 3(d–f) as compared with figure 3(a–c) for $Pe = 64$. For $Pe \sim O(1)$, Brownian fluctuations induce a chaotic behaviour whereby the platelet rotates frequently and randomly. In this range, the trajectories for a purely imaginary and a real k_e are practically indistinguishable (see $Pe = 6.4$ in figure 3).

Figure 3 suggests that for large Pe, the rotational dynamics depends strongly on whether k_e is real or purely imaginary, while for smaller Pe such dependency disappears.

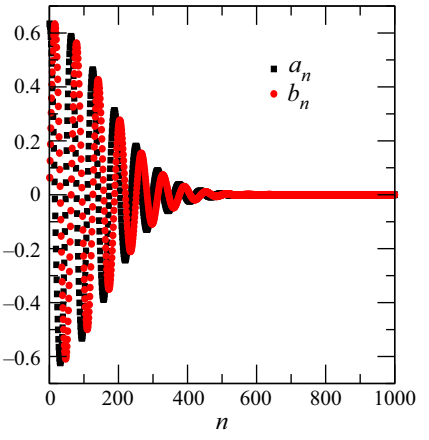

Figure 4. Spectral coefficients a_n and b_n for $k_e = 0.05\mathrm{i}$ and $Pe = 10^6$ and $t \to \infty$. The spectral coefficients are truncated at $n = 1000$, since $a_n, b_n \to 0$ above this threshold.

Quantifying the values of Pe needed for the rotational dynamics to depend on the value of k_e requires solving the Fokker–Planck (2.1).

3.1.1. *Time evolution of the orientation distribution function's moments*

Taking advantage of the periodicity of $p(\phi, t)$, any solution of (2.1) can be expressed as a spectral series,

$$p(\phi, t) = a_0(t) + \sum_{n=1}^{\infty} \left[a_n(t) \cos(2n\phi) + b_n(t) \sin(2n\phi)\right]. \tag{3.2}$$

Normalisation of p requires $a_0 = 1/\pi$, and assuming ϕ to be uniformly distributed at time $t = 0$ gives an initial uniform distribution $p(\phi, 0) = 1/\pi$. In spectral coordinates, this is equivalent to having only one non-zero coefficient $a_0 = 1/\pi$. Numerically, we solve (2.1) by truncating the series at a large value N, yielding $2N$ first-order differential equations for the spectral coefficients (Leahy *et al.* 2015). A truncated value $N = 1000$ has been chosen from the analysis of the spectral coefficients a_n and b_n. For $n > N$, $a_n, b_n \to 0$ for all values of time t (see figure 4 for $t \to \infty$). The $2N$-coupled equations are solved in time by a Runge–Kutta method (Press *et al.* 2007). The mean angle, standard deviation and higher moments can be evaluated directly in terms of the spectral distribution. For example, the mean and variance are

$$\mu = \langle\phi\rangle = \sum_{i=1}^{\infty} \frac{\pi}{2n}(-1)^{1+n} b_n, \quad \sigma^2 = \left\langle(\phi - \mu)^2\right\rangle = \frac{\pi^3}{12} + \sum_{i=1}^{\infty} \frac{\pi}{2n^2}(-1)^n a_n - \mu^2, \tag{3.3a,b}$$

respectively. Here, the close brackets $\langle\ \rangle$ represent an average over the orientation distribution function $p(\phi, t)$ for fixed t.

Many studies discuss solutions to (2.1) for elongated particles with real k_e (Burgers 1938; Peterlin 1938; Sadron 1953; Scheraga 1955; Leal & Hinch 1971; Hinch & Leal 1972, 1973; Férec *et al.* 2008; Leahy *et al.* 2015; Leahy, Koch & Cohen 2017). However, the case of purely imaginary k_e, to our knowledge, has not yet been analysed. The time evolution of the mean, variance and third-order moment $\left\langle(\phi - \mu)^3\right\rangle$ of the orientation distribution for

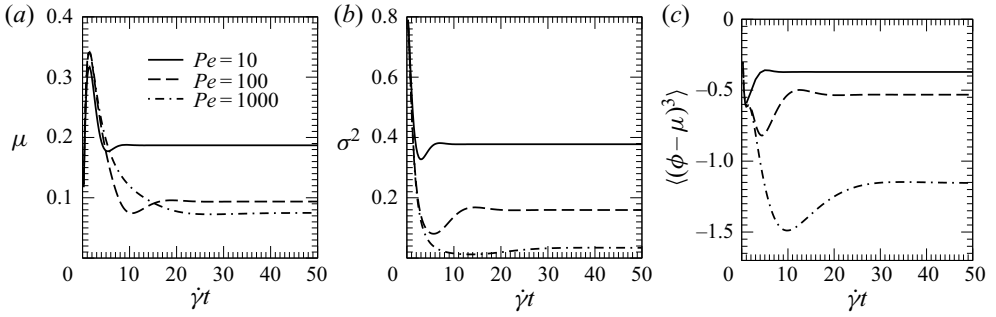

Figure 5. Mean (*a*), variance (*b*) and skewness (*c*) of the angular probability distribution versus time, for a nanoplatelet with $k_e = 0.1\mathrm{i}$ and different values of *Pe*.

$k_e = 0.1\mathrm{i}$ and different *Pe* is shown in figure 5. Similarly to when k_e is real (Leahy *et al.* 2015), the moments relax in time to a steady value, with a relaxation time that decreases as *Pe* decreases. Therefore, we can assume that the statistical steady state is reached over a time greater than the relaxation time $P_R = \dot{\gamma}^{-1}(|k_e|^{-1} - |k_e|)$ of a platelet in absence of Brownian motion.

3.2. *Steady-state probability distribution*

We solve (2.1) with $\dot{p} = 0$ to find the steady-state orientation distribution function $p(\phi)$ using the method described in § 3.1.1. The effect of *Pe* on $p(\phi)$ comparing real and purely imaginary values of k_e is shown in figure 6. For $Pe = 1000$, there is a noticeable difference in the shape of the orientation distribution function depending on whether k_e is real or purely imaginary. In particular, $p(\phi)$ has a much sharper peak if k_e is purely imaginary. This difference can be analysed by considering the limit $Pe \to \infty$. For $Pe \to \infty$, (2.1) reduces at steady state to

$$p\Omega = c, \tag{3.4}$$

for some integration constant c. For real k_e, normalisation of p gives $p = (P\dot{\gamma}|\Omega|)^{-1}$, where P is the time period (see (2.6)) (Anczurowski & Mason 1967*a*). Such a probability distribution shown by the (red) dotted line in figure 6 has mean orientation angle $\mu = 0$ and finite variance σ^2 by the symmetry of p about $\phi = 0$. If k_e is purely imaginary, however, $1/\Omega$ diverges as $\phi \to \pm\phi_c$, and thus the integrand of c/Ω will not be finite unless $k_e = 0$ or $c = 0$, as required by the normalisation constraint for p. Thus, the equation $p\Omega = c$ is only satisfied for $c = 0$ and $p(\phi) = \delta(\phi - \phi_c)$, as expected. As seen in figure 6 for the imaginary k_e, as *Pe* increases the probability distribution function indeed converges to a Dirac delta, confirming that for sufficiently large *Pe* the platelet spends most of the time fluctuating about ϕ_c (as observed in figure 3*d–f*).

For $Pe = 10$ the orientation distribution functions for $k_e = 0.1$ and $k_e = 0.1\mathrm{i}$ are almost identical, and slightly skewed towards positive values of ϕ (the value of μ, σ^2 and $\langle(\phi - \mu)^3\rangle$ for $k_e = 0.1$ and $k_e = 0.1\mathrm{i}$, given in the caption of figure 6, are within 10 % of each other). Since *Pe* is not small in this example, hydrodynamic stresses must play a role in creating such skewness. However, the effect of changes to the value of k_e due to surface slip on the probability distribution is evidently minor.

Balancing the orders of magnitude of the convective and diffusive fluxes appearing in (2.1) yields a characteristic angle Φ. From this, we can define a 'local' *Pe* number, $Pe_{loc} = \dot{\gamma}\Omega(\phi)\Phi/D_r$ (Leal & Hinch 1971). The effects of Brownian fluctuations on the orientation

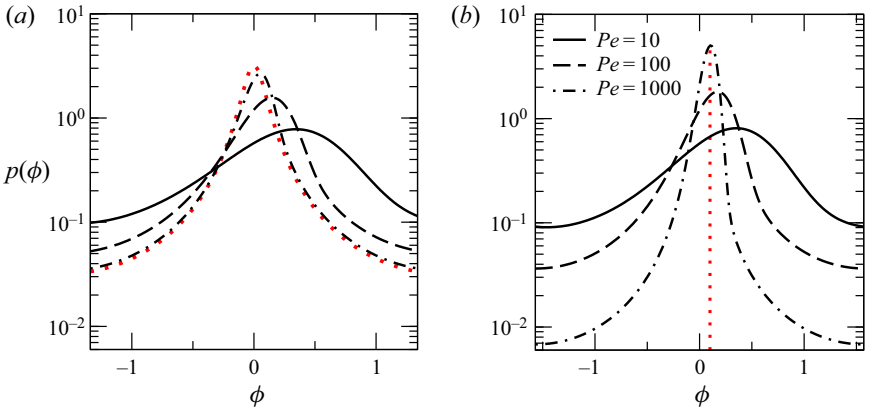

Figure 6. Steady-state orientation distribution function $p(\phi)$ for a real ($k_e = 0.1$) or a purely imaginary ($k_e = 0.1$i) value of k_e for different Pe numbers. The red dotted line marks the orientation distribution function for $Pe \to \infty$ and $k_e = 0.1$ (a) and the location of ϕ_c for $k_e = 0.1i$ (b). The values $[\mu, \sigma^2, \langle(\phi - \mu)^3\rangle]$ in increasing order of Pe are [0.17, 0.39, −0.36], [0.069, 0.21, −0.40] and [0.019, 0.14, −0.30], respectively, for $k_e = 0.1$; and [0.19, 0.38, −0.37], [0.094, 0.16, −0.53] and [0.075, 0.033, −1.1], respectively, for $k_e = 0.1$i.

of the platelets are considered to be 'weak' compared with the hydrodynamic angular velocity if, for ϕ near zero, $Pe_{loc} \gg 1$ (Leal & Hinch 1971). This condition translates to the Brownian angular velocity being smaller than, using (2.3), $|\Omega| \sim k_e^2$. For $|\Omega| \sim k_e^2$ we have that ϕ can be at most $\Phi \sim |k_e|$, and so $|Pe_{loc}|$ can be at most of the order of $|k_e^3 Pe|$.

Thus, for $Pe \gg |k_e|^{-3}$ Brownian diffusion is subdominant, and the rotation of the platelet can be approximated by the orientation distribution obtained for negligible Brownian fluctuations.

To quantify the value of Pe for which the orientation distribution does not depend on k_e to leading order, one can proceed as follows. For a geometric aspect ratio $k \to 0$, we will verify in § 4 that $|k_e| \ll 1$ whatever the value of λ. Expanding the right-hand side of the equation for $\dot{\phi}$ in (2.3) to leading order in $|k_e|$, the hydrodynamic velocity is seen to become independent of k_e if $\sin^2\phi_m \gg |k_e^2| \cos^2\phi_m$. Thus, because we are interested in a critical Pe valid for both $\lambda = 0$ and finite λ, the condition for ϕ_m is $\tan\phi_m \approx \phi_m \gg \max(|k_e(\lambda = 0)|, |k_e(\lambda)|)$. For the rotational dynamics to be independent of k_e to leading order, the local Péclet number must be $O(1)$ over the characteristic angle $\Phi \sim \phi_m$. This regime is associated with a rotational velocity $\Omega(\phi_m) \approx \dot{\gamma}\phi_m^2$, so the local Péclet number $Pe\phi_m^3 \sim 1$. It follows from the condition $\phi_m \gg \max(|k_e(\lambda = 0)|, |k_e(\lambda)|)$ that $Pe \ll \min(|k_e^{-3}(\lambda = 0)|, |k_e^{-3}(\lambda)|)$. Thus, Brownian diffusion will control the orientation of the platelet when $Pe \ll \min(|k_e^{-3}(\lambda = 0)|, |k_e^{-3}(\lambda)|)$.

The value $Pe_m = \min(|k_e^{-3}(\lambda = 0)|, |k_e^{-3}(\lambda)|)$ is an important threshold. For $Pe \ll Pe_m$ the value of k_e does not affect to leading order the orientation distribution $p(\phi, t)$. When $Pe \gg Pe_m$ significant changes to the orientation distribution for either a real or purely imaginary value of k_e are expected. Figure 7 demonstrates the importance of this threshold on the statistical moments μ, σ^2 and $\langle(\phi - \mu)^3\rangle$. The black line corresponds to $Pe_m = |k_e|^{-3}$. For Pe above this line, the statistical moments approach the values predicted by using the probability distribution functions corresponding to $Pe \to \infty$. In this case the moments depend strongly on the value of k_e. For example, if k_e is purely imaginary, then the variance $\sigma^2 \to 0$ and the mean $\mu \to k_e$ for Pe above the $Pe_m = |k_e^{-3}|$ line. If instead k_e is real then σ^2 is instead finite and $\mu \to 0$. Likewise, if Pe is much smaller than $|k_e^{-3}|$ the

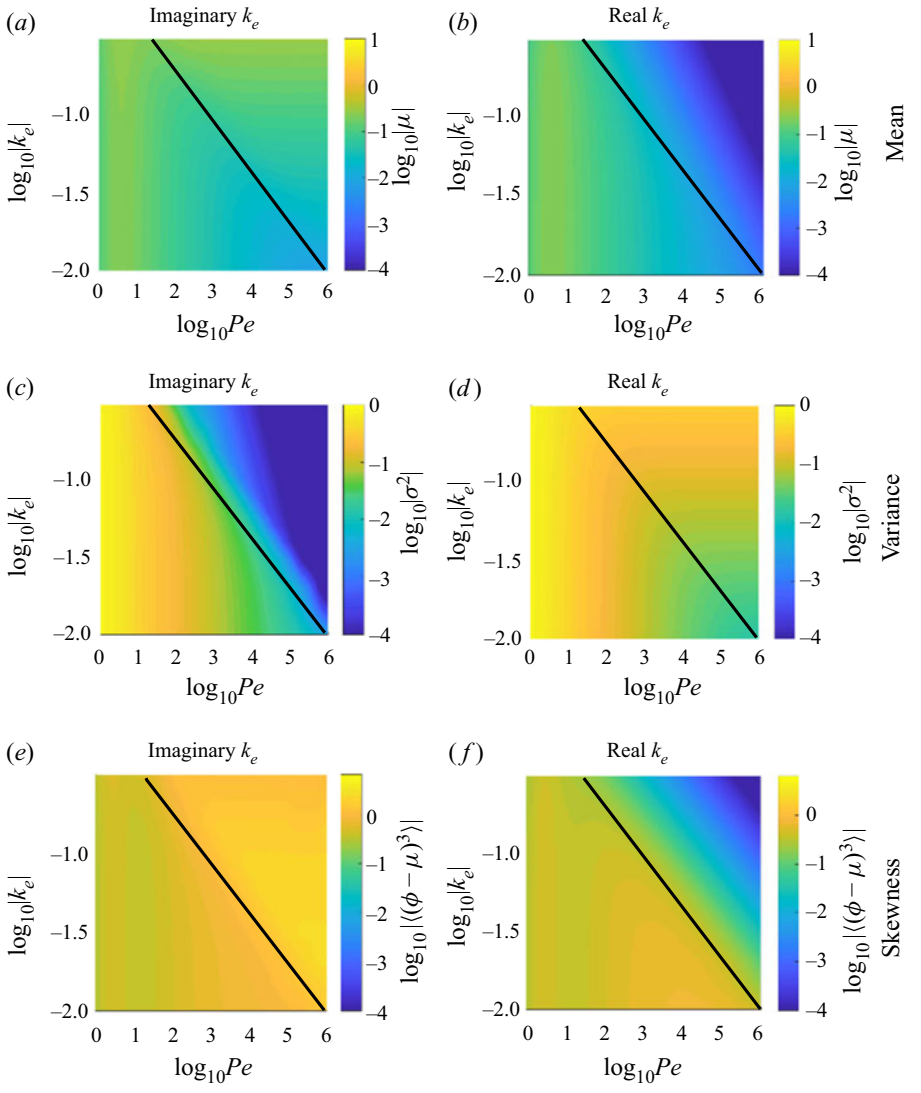

Figure 7. Colour maps of the mean μ, variance σ^2 and skewness $\langle(\phi-\mu)^3\rangle$ of the steady-state orientation distribution in the (Pe, k_e) space. The black straight line is $Pe = |k_e|^{-3}$. For Pe above this line, the difference in the moments between real and purely imaginary values of k_e becomes noticeable.

statistical moments depend only on Pe and become essentially independent of k_e (compare, for example, the colour maps for $|k_e| \leq 0.1$ and $Pe \leq 100$ in figure 7).

Finally, for $Pe \ll 1$, the platelet's rotation is almost entirely due to Brownian diffusion. As $Pe \to 0$, the leading-order orientation distribution can be described at all times by a uniform distribution (Burgers 1938; Peterlin 1938; Scheraga 1955). Such distribution describes randomly rotating platelets that complete an average rotational cycle with a variance much larger than in the pure hydrodynamic flow limit, as also shown in figure 3.

3.3. *Threshold Péclet number for full rotations*

When the effective aspect ratio k_e is purely imaginary, we can define a critical Péclet number Pe_c separating the stable region, in which the platelet fluctuates about ϕ_c, from the

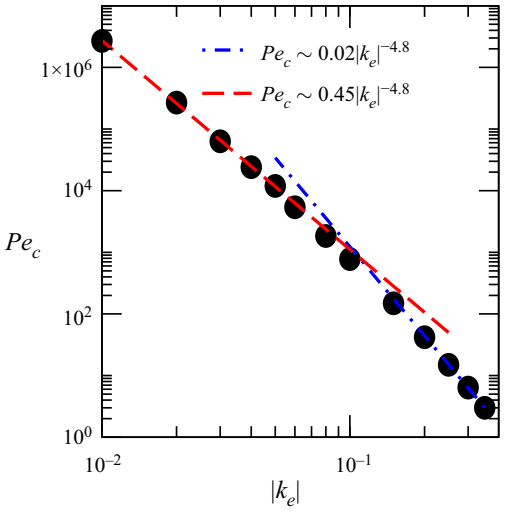

Figure 8. Threshold value of the Péclet number Pe_c beyond which no platelet rotation is expected, as a function of $|k_e|$ (with k_e purely imaginary). Black disks are numerical values, lines are fits for $|k_e| \gtrapprox 0.1$ (dot–dashed blue line) and $|k_e| \lessapprox 0.1$ (dashed red line), respectively.

unstable region in which the platelet performs full rotations. Because the hydrodynamic angular velocity is zero for $\phi = \phi_c$ and small in the neighbourhood of this critical angle, in the stable region weak Brownian fluctuations always affect the orientation of the platelet for any finite value of Pe. When the platelet is in the unstable region, full rotation cycles can occur because the variance σ^2 is large enough for the fluctuating platelet to 'jump out' of the region where $\Omega(\phi)$ is positive. The width of this 'hydrodynamic potential well' is given by the range of values of ϕ for which $\Omega(\phi)$ is positive. This width can be approximated as $2\arctan(\theta_c) \approx 2|k_e|$ for $|k_e| \ll 1$. Therefore, we estimate that the probability for a given particle to perform full rotary cycles becomes significant for σ larger than a threshold $\sigma \sim 2|k_e|$.

Using our numerical procedure for calculating σ^2, as given in (3.3*a*,*b*), we calculate Pe_c by first computing $\sigma(Pe, k_e)$ and then calculating the value of Pe that gives $\sigma = 2|k_e|$. We emphasise that full rotations of a given platelet can still occur for Pe significantly larger than Pe_c, but these events, associated with the tails of the probability distribution, are rare and should not affect the occurrence of a stable orientation on account of the approximate symmetry of $p(\phi)$ about its mean value. Our results for Pe_c are shown in figure 8 for a range of purely imaginary k_e. As $|k_e|$ decreases, the width of the 'hydrodynamic potential well' decreases, so Pe_c increases. The data appear to be well fitted by $Pe_c \propto |k_e|^{-3.4}$ for small values of $|k_e|$. The exponent -3.4 is quite close to the exponent -3 obtained by balancing the order of magnitude of the convection and diffusive terms in (2.1). The data are expected to approach this theoretical value for values of $|k_e|$ smaller than we could simulate. For $|k_e| \gtrapprox 0.1$ the local power-law exponent is definitely not close to -3. In this region, the line $Pe_c \propto |k_e|^{-4.8}$ appears to be a better fit to the data.

Figure 8 does not enable us by itself to draw a conclusion about whether a stable orientation occurs for given values of λ and a, as both k_e and Pe depend on these variables. To draw such conclusion we need to map k_e and Pe to specific values of λ and a. This will be done in the next section, by considering particles of a specific geometry and slip properties.

4. Rotational dynamics of model graphene-like nanoplatelets

Our work is motivated by understanding the dynamics of graphene colloids or similar 2-D nanomaterials. Applying our theory to realistic graphene-like nanoplatelets requires evaluating k_e for geometric and slip characteristics typical of this specific type of anisotropic colloid. The calculation of k_e for platelets of atomic thickness (in the following we will use the word 'nanoplatelets' for brevity) must be done with care, because the classical framework developed for mesoscale colloidal particles may break down when one of the particle dimensions is comparable with the size of the liquid molecules. In previous studies (Gravelle, Kamal & Botto 2020; Gravelle, Kamal & Botto 2021; Kamal *et al.* 2020), we have performed MD of a rigid graphene nanoplatelet suspended in a shear flow of water and other solvents. We showed that k_e can still be predicted using a continuum description, provided that the hydrodynamic stress is computed on a suitable reference surface surrounding the platelet and a slip boundary condition is enforced at this surface. Interestingly, we found that using a single slip parameter λ is sufficient to capture the effects of the hydrodynamic slip on the particle rotation and hydrodynamic torque, despite the heterogeneous surface of graphene (which has different slip properties at the edges as compared with the planar region). This feature, which we have proved to be related to the weak sensitivity of the hydrodynamic torque on the tangential components of the traction at the edges, is useful as it simplifies the analysis of the problem by reducing the number of parameters.

4.1. *Effective nanoplatelet's geometry*

Nanoplatelets of 2D materials, made for example of carbon (C), boron nitride (BN), or molybdenum disulfide (MoS_2), are essentially stacks of atomic crystal layers. To achieve a continuum description of the nanoplatelets in flow, one must define the reference surface that best approximates such platelets from a hydrodynamic standpoint. Molecular dynamics calculations reveal that, because of the smoothing of the molecular flow field by the finite-interaction potential near the edges, the reference surface is a cuboid with rounded edges, as sketched in figure 9. The cuboid has a half-thickness $b = \xi + d_{gg}(n - 1)/2$, where ξ is the effective radius of a single atom of the nanoplatelet, d_{gg} is the interlayer spacing and n is the number of stacks. For multilayer graphene, $d_{gg} \approx 3.35$ Å (Chung 2002). The effective radius ξ depends on the equilibrium distance between the atoms of the solid and the liquid molecules. For graphene in water, $\xi \sim 1.8$–2.5 Å (Gravelle *et al.* 2014), and comparable values can be expected for BN and MoS_2 due to their similar atomic structure (Radisavljevic *et al.* 2011; Tocci *et al.* 2014; Luan & Zhou 2016). The edges form a semicircle shape for $n = 1$ (figure 9*a*) and a flat face with blunt edges as n increases (figure 9*b–d*). The shape of the edge slightly affects the value of k_e: the blunter the edge, the larger the value of k_e for a fixed aspect ratio a/b (cf. Singh *et al.* (2014) for $\lambda = 0$).

4.2. *Range of slip lengths*

For atomically smooth surfaces of 2-D nanomaterials such as graphene, the hydrodynamics slip length measured at the planar surface of the particle ranges from a few nanometres to tens of nanometres. As summarised in table 1, experiments performed on graphite (Maali *et al.* 2008; Ortiz-Young *et al.* 2013), and *ab initio* calculations (Tocci *et al.* 2014), suggest $\lambda \approx 10$ nm for water and graphene. In the case of NMP or ethanol, the slip length of graphene is also relatively large (>10 nm) (Gravelle *et al.* 2020). Ionic liquid (IL)

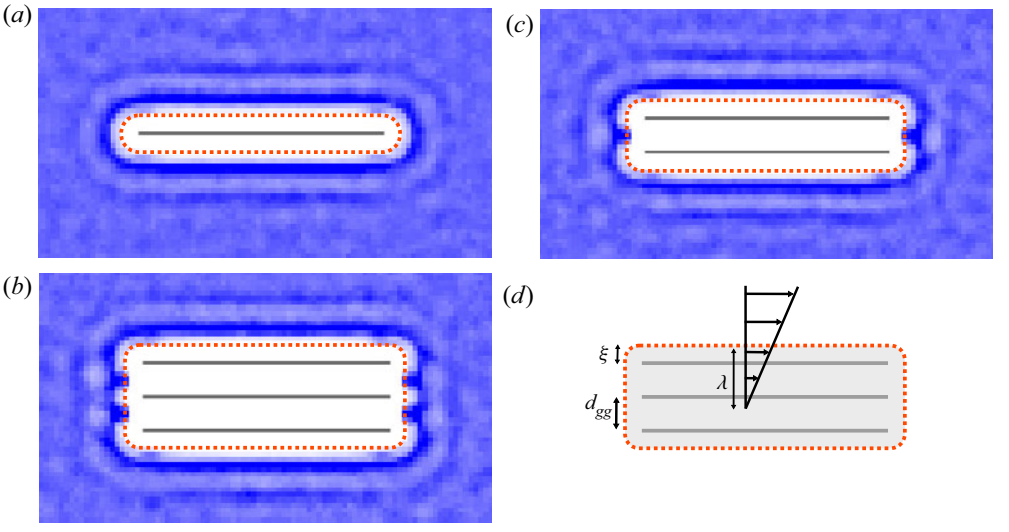

Figure 9. (*a–c*) Water density profiles as extracted from MD simulations for a number of layer $n = 1$ (*a*), 2 (*b*) and 3 (*c*), respectively. The centres of the carbon atoms are located along the grey lines. Details of the molecules dynamics simulations are given in Kamal *et al.* (2020). The colour field is the water density, from white (low density) to blue (high density), and the red dashed lines show the reference surfaces. (*d*) Sketch of the reference surface for $n = 3$, showing the slip length λ, the effective radius ξ of the carbon atoms and the interlayer spacing d_{gg}.

can also give large slip lengths, but in this case λ has been found to depend strongly on the shear rate (Voeltzel *et al.* 2018).

The slip length λ can also be significant for atomically smooth and chemically homogeneous materials other than graphene. The interaction of BN and water gives $\lambda \sim 3$ nm (Tocci *et al.* 2014). While this value may seem small, it is still larger than the thickness of single-layer BN. Despite the large scatter in the literature data for λ, consequence of the dependence of MD simulation results on empirical force fields, table 1 suggests that relatively large slip lengths are not uncommon in 2-D nanomaterials, which is essentially a consequence of the fact than many 2-D nanomaterials have atomically smooth surfaces. To provide theoretical guidelines on a range of realistic values, characteristic of those in table 1, we will evaluate the rotational dynamics of nanoplatelets for $\lambda = 0$, 2, 20 and 200 nm.

4.3. *Calculation of k_e and D_r*

Using a boundary integral method which will be described shortly, we have calculated the effective aspect ratio k_e and the rotational diffusion coefficient D_r for typical nanoplatelets by solving the incompressible Stokes equations

$$\nabla \cdot \boldsymbol{\sigma} = 0, \quad \nabla \cdot \boldsymbol{u} = 0, \tag{4.1a,b}$$

where $\sigma_{ij} = -\delta_{ij}p + \eta(\partial u_i/\partial x_j + \partial u_j/\partial x_i)$ is the hydrodynamic stress with p the pressure and η the viscosity; $\boldsymbol{u}$ is the velocity field. For the reference surface, we use a cuboid with rounded edges (§ 4.1). At the reference surface of the platelet we prescribed the Navier slip boundary condition

$$\boldsymbol{u}_{sl} = \frac{\lambda}{\eta}\boldsymbol{n} \times \boldsymbol{f} \times \boldsymbol{n}, \tag{4.2}$$

Material	Liquid (η (mPa s))	λ (nm)	Method	Reference
graphene	water (1.0)	10.4 ± 2.2	*ab initio* MD	Tocci *et al.* (2014)
graphene	water (1.0)	60 ± 5	MD	Kamal *et al.* (2020)
graphene	water (1.0)	$[1 - 80]$	MD	Kannam *et al.* (2013)
graphene	water (1.0)	83	MD	Falk *et al.* (2012)
graphene	decane (0.85)	103	MD	Falk *et al.* (2012)
graphene	OMCTS (1.0)	18	MD	Falk *et al.* (2012)
graphene	ethanol (1.1)	250	MD	Falk *et al.* (2012)
graphene	ethanol (1.1)	30 ± 3	MD	Falk *et al.* (2012)
graphene	NMP (1.6)	14 ± 2	MD	Kamal *et al.* (2020)
graphene	CPO (1.3)	45 ± 2	MD	Kamal *et al.* (2020)
graphite	IL ($[1 - 200]$)	$[300 - 10\,000]$	MD	Voeltzel *et al.* (2018)
graphite	water (1.0)	8	experiment	Maali *et al.* (2008)
graphite	water (1.0)	12 ± 3.3	experiment	Ortiz-Young *et al.* (2013)
DlC	water (1.0)	0.55 ± 1.37	experiment	Ortiz-Young *et al.* (2013)
DlC	IL ($[1 - 200]$)	$[1 - 100]$	MD	Voeltzel *et al.* (2018)
MoS_2	water (1.0)	5.6	MD	Luan & Zhou (2016)
mica	water (1.0)	< 2	experiment	Maali *et al.* (2008)
mica	water (1.0)	~ 0	experiment	Ortiz-Young *et al.* (2013)
BN	water (1.0)	3.3 ± 0.6	*ab initio* MD	Tocci *et al.* (2014)
GO	water (1.0)	0.34 ± 0.38	experiment	Ortiz-Young *et al.* (2013)
silicon	water (1.0)	1 ± 1.7	experiment	Ortiz-Young *et al.* (2013)

Table 1. Literature values of the slip length for different solid material/solvent combinations. The materials and liquids are: diamond-like carbon (DIC); graphene oxide (GO); boron nitride (BN); molybdenum disulfide (MoS_2); ionic liquid (IL); n-methyl-2-pyrrolidone (NMP); octamethylcyclotetrasiloxane (OMCTS); cyclopentanone (CPO). *Ab initio* MD refers to a method allowing for the calculation of electronic behaviour from first principles by using a quantum mechanical method.

where $\boldsymbol{f} = \boldsymbol{\sigma} \cdot \boldsymbol{n}$ is the hydrodynamic surface traction and $\boldsymbol{n}$ is the unit normal vector (Lauga, Brenner & Stone 2008). In the present case, the macroscopic time scale is given by the rotational time period $P_R = \dot{\gamma}^{-1}(|k_e|^{-1} + |k_e|)$, which is controlled by the particle aspect ratio and by the shear rate. For realistic parameters, P_R is always much larger than the time scale of the microscopic motion of the fluid molecules, which is typically of the order of picoseconds. A boundary integral equation is used to calculate the distribution of $\boldsymbol{f}$ corresponding to each given inclination angle ϕ (Pozrikidis 1992). Denoting the reference surface by S, the boundary integral equation for a point $\boldsymbol{x} \in S$ is (Luo & Pozrikidis 2008)

$$\int_S \boldsymbol{n} \cdot \boldsymbol{K}(x', y') \cdot \boldsymbol{u}_{sl}\, \mathrm{d}S - \frac{1}{\eta} \int_S \boldsymbol{G}(x', y') \cdot \boldsymbol{f}\, \mathrm{d}S = \frac{\boldsymbol{u}_{sl}(\boldsymbol{x})}{2} - \boldsymbol{u}_\infty(\boldsymbol{x}), \tag{4.3}$$

where the integral is over the surface parameterised by the coordinate point $\boldsymbol{x}_1 = (x_1, y_1)$. In (4.3), $x' = x_1 - x$, $y' = y_1 - y$; $\boldsymbol{G}$ and $\boldsymbol{K}$ are Green's functions corresponding to the 2-D 'Stokeslet' and 'Stresslet', respectively; $\boldsymbol{u}_\infty$ is the undisturbed simple shear flow field. The traction is used to calculate the hydrodynamic torque $T(\phi) = \hat{\boldsymbol{e}}_z \cdot \int [\boldsymbol{x} \times \boldsymbol{f}]\, \mathrm{d}S$ acting on the fixed platelet. In order to achieve high accuracy with the boundary integral algorithm, a non-uniform grid has been implemented with the surface of the particle being divided into two regions, see figure 10(*a*). Namely, the edge region, made of the edges of arclength S_E plus the neighbouring regions of lengths $S_E/4$, and the planar region. The total number of grid points, N, is distributed between the two regions, with the number of points of the edge region being $N/2$ up to a maximum of 32 points for each end. Following a convergence

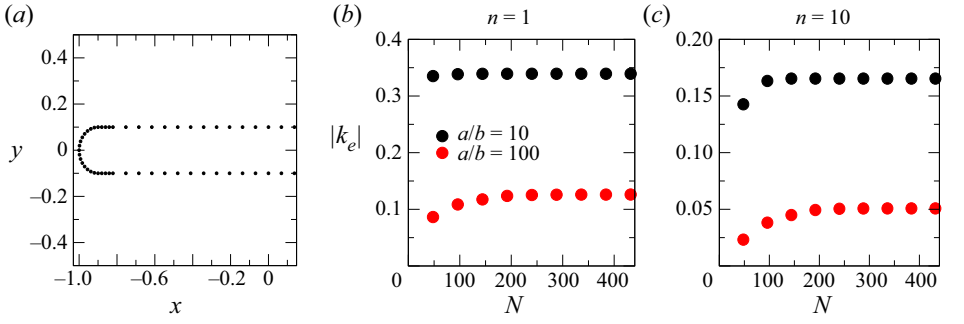

Figure 10. (*a*) Example of the discretisation of a $n = 1$ surface with $N = 96$. (*b*,*c*) Effective aspect ratio $|k_e|$ versus the number of discretisation points N for platelets with $\lambda = 20$ nm, $a/b = 10$ or $a/b = 100$, and either $n = 1$ (*b*) or $n = 10$ (*c*).

analysis (figure 10*b*,*c*), we set $N = 288$ for platelets with $a/b \leq 100$ and $N = 384$ for platelets with $a/b > 100$; the value of k_e is then calculated from (2.4).

The (4.3) is evaluated numerically by using the following method. First, the traction and slip velocity are discretised as N piecewise constant functions $\{\boldsymbol{f}[1] \dots \boldsymbol{f}[N]\}$ and $\{\boldsymbol{u}^{sl}[1] \cdots \boldsymbol{u}^{sl}[N]\}$, respectively, each associated with a surface element $S_i = \int_{s_i}^{s_{i+1}} \mathrm{d}S$. With this discretisation, for each point s_j for $j = \{1 \cdots N\}$, the discretised form of (4.3) becomes (Kamal *et al.* 2020)

$$\sum_{i=1}^{N} \left[\boldsymbol{u}_{sl}[i] \cdot \int_{s_i}^{s_{i+1}} \boldsymbol{K}(s, s_j) \cdot \boldsymbol{n}(s)\, \mathrm{d}S(s) - \frac{\boldsymbol{f}[i]}{\eta} \cdot \int_{s_i}^{s_{i+1}} \boldsymbol{G}(s, s_j)\, \mathrm{d}S(s) \right] = \frac{\boldsymbol{u}_{sl}(s_j)}{2} - \boldsymbol{u}_{\infty}(s_j). \tag{4.4}$$

For $i \neq j$, each subintegral is evaluated using a Gauss–Legendre quadrature method. If $i = j$, the integrands are singular. The singular integrand containing the $\boldsymbol{G}$ tensor is evaluated by using a specific quadrature method for logarithmic singularities (Pozrikidis 2002), and the singular integrand containing the $\boldsymbol{K}$ tensor is evaluated analytically by Taylor expansion about the singular point (Kamal *et al.* 2020). Equation (4.2) provides a closed relation between $\boldsymbol{u}_{sl}$ and $\boldsymbol{f}$, and thus (4.4) can be arranged into a closed system of N linear equations for each component of the traction $f_i[j]$. This system is solved for $f_i[j]$ by using Gaussian elimination. To test the accuracy of our implementation, we compared the predicted value of k_e with the corresponding exact solution for circular cylinder in shear flow (Kamal *et al.* 2020). This test confirms the expected second-order spatial convergence.

The rotational diffusion coefficient of a particle is given by $D_r = k_B T / F_r$, where k_B is the Boltzmann's constant, T is the absolute temperature and F_r is the rotational drag coefficient. The rotational drag coefficient is also calculated via the boundary integral method, by calculating the hydrodynamic torque exerted on the fluid by a platelet rotating with velocity $\boldsymbol{u} = \hat{\boldsymbol{e}}_z \times \boldsymbol{x}$ in a fluid otherwise at rest. In agreement with the result of Sherwood (2012) for a disk, we find for our model platelet that F_r is independent of slip as $k \to 0$. In this limit we found $F_r \approx c_1 \eta a^3$, where $c_1 = 6.29 \pm 0.02$ (to be compared with $c_1 = 32/3$ for a 3-D disk of zero thickness (Leal & Hinch 1971; Sherwood 2012), and to $c_1 = 2\pi$ for an infinite plate of zero thickness (Sherwood & Meeten 1991)). The second-order accuracy in the computation of D_r was assessed by comparing against the exact solution for D_r for a cylinder with a Navier slip boundary condition, as done by Luo & Pozrikidis (2008) for a sphere.

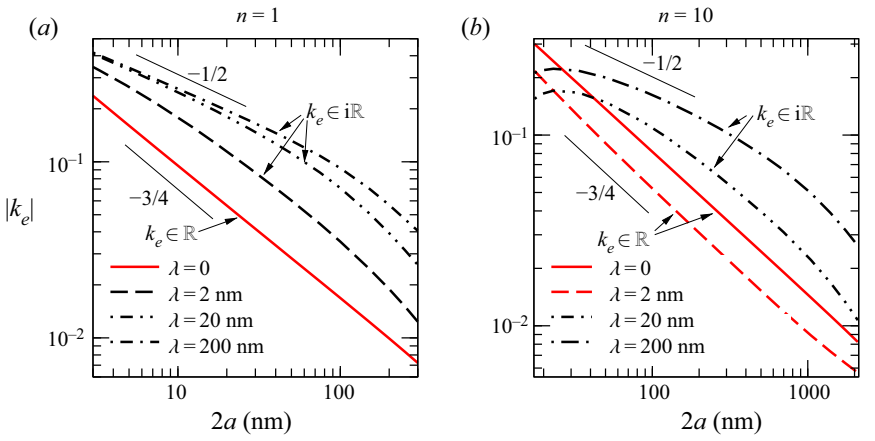

Figure 11. Absolute value of the effective aspect ratio k_e versus the platelet length $2a$ for $\xi = 0.25$ nm and for $n = 1$ (*a*) and $n = 10$ (*b*). The black lines correspond to the purely imaginary values of k_e and the red lines to real values of k_e.

Values of k_e for our model platelet with $\xi = 0.25$ nm, slip length $\lambda = 0$, 2, 20 and 200 nm, and $n = 1$ or 10 are shown in figure 11. We limit our calculations to aspect ratios $k \geq 0.001$, because using $k < 0.001$ leads to large numerical error owing to severe resolution requirements. For $\lambda = 0$, the effective ratio of the platelet follows the power law relationship $k_e \sim g_n k^{3/4}$, with g_n a prefactor that depends on n. This power law relationship is the same as for disks with 'blunt edges' (Singh, Koch & Stroock 2013). We find $g_1 \approx 0.91$ for $n = 1$ and $g_{10} \approx 1.0$ for $n = 10$. As λ increases, however, the relation between k_e and k is not necessary a power law, as shown for $\lambda = 2$, 20 and 200 nm for $n = 1$, and $\lambda = 20$ and 200 nm for $n = 10$. In the limit $\lambda/a \gg 1$, the value of k_e can be analytically approximated as $k_e \propto i\sqrt{k}$ (Kamal *et al.* 2020), as confirmed in figure 11 for platelet length $2a \lessapprox 20$ nm, $n = 1$ and $\lambda = 20$ nm and 200 nm (we remark, however, that most applications of nanoplatelets typically involve $\lambda < a$).

As the slip length increases, the value of k_e^2 decreases and changes sign at some critical value λ_c (figure 12). An explanation for this is the following. Calculating k_e requires the evaluation of the total hydrodynamic torque on a fixed platelet for two angles: $\phi = 0$ and $\phi = \pi/2$. The total torque for $\phi = 0$ is more sensitive to λ than the torque for $\phi = \pi/2$, because slip affects primarily the flow moving in the direction tangential to the surface of the particle. Thus, predicting λ_c essentially requires predicting the angle for which $T(0)$ changes sign. When $\lambda = 0$, in an asymptotic expansion in powers of b, the $O(b)$ contribution to $T(0)$ turns out to be zero, because of an exact cancellation between torque contributions due to normal and tangential stresses. This cancellation results in a 'clockwise' torque that is second-order in the thickness, $T \propto b^2$; the second-order tangential traction determining this torque is $f_x^{(2)} \propto b$ (Singh *et al.* 2014). The effect of slip over the flat surface of the platelet is to reduce the tangential traction f_x, without changing significantly the normal traction f_y (figure 13). An analysis for $\lambda/a \ll 1$ shows that the effect of slip is to reduce f_x by an amount of $O(\lambda)$, resulting in a second-order traction $f_x^{(2,sl)} \propto \lambda$ (Kamal *et al.* 2020), where '*sl*' indicates that this traction is due to slip. The total torque $T(0)$ changes sign when $f_x^{(2,sl)} > f_x^{(2)}$. This condition occurs at a threshold value $\lambda_c \approx h_n b$, where h_n is a numerical prefactor that depends on the number of layers n (Kamal *et al.* 2020). For $n = 1$, our numerical procedure gives $h_1 \approx 0.8$, and $b \approx 0.25$ nm

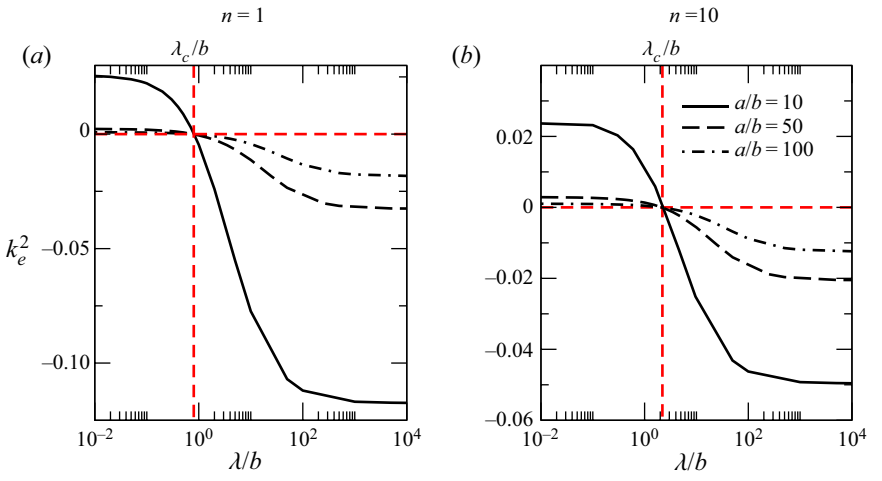

Figure 12. Effective aspect ratio k_e^2 versus the slip length λ for different platelet lengths $2a$. The half-thickness of the platelet is $b \approx 0.25$ nm and $b \approx 1.75$ nm for $n = 1$ and $n = 10$, respectively. Red dashed lines mark the positions where k_e^2 changes sign.

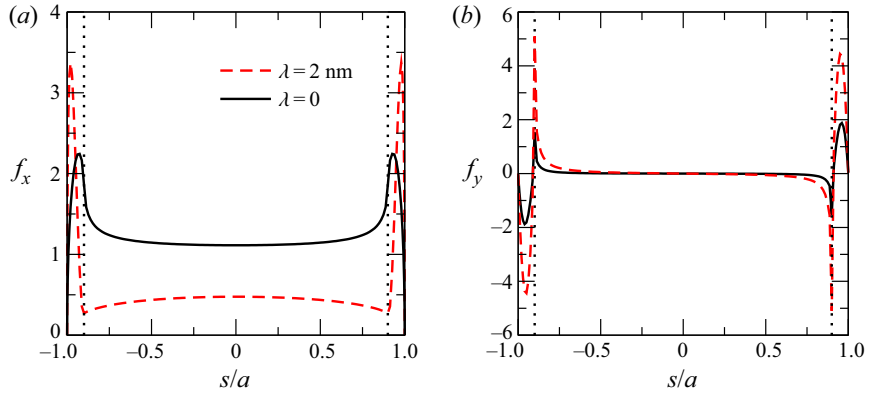

Figure 13. The streamwise (a) and normal (b) hydrodynamic traction distribution along the surface of a platelet fixed at an orientation $\phi = 0$ for $n = 1$ and $a/b = 10$. The vertical dotted line marks the position of the edge of the platelet.

so $\lambda_c \approx 0.2$ nm. For $n = 10$, $h_{10} \approx 2.2$ and $b \approx 1.75$ nm so $\lambda_c \approx 3.85$ nm (figure 12). For moderate-to-large values of λ/b, slip can have a marked effect on the traction at and near the edges of the platelet (the position of the edge is marked by the dotted vertical line in figure 13). This traction can significantly affect k_e for larger values of λ so that k_e is in general a non-trivial function of λ. Comparison of the traction and $T(0)$ with MD simulations reveals that the approximation of a uniform surface slip over the surface of the platelet still gives accurate predictions of k_e even when λ/b is large (Kamal *et al.* 2020). In the following, since k_e is a non-trivial function of λ, b and a (figure 12), we will use the numerically computed values of k_e.

4.4. *Regimes of rotation*

Here we analyse the effect of the Péclet number, comparing the rotational dynamics of nanoplatelets with and without surface slip. We first compare the cases $\lambda = 0$ (no-slip) and

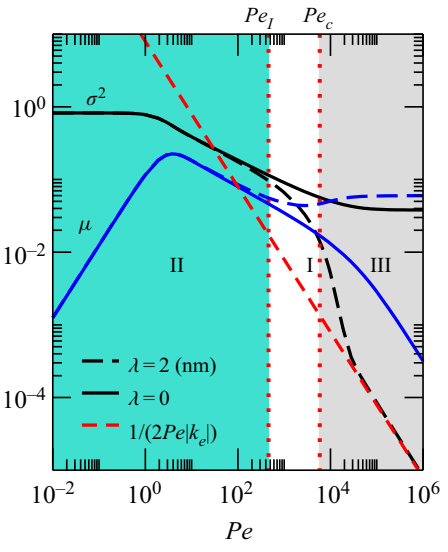

Figure 14. Comparison of mean and variance of the fluctuating rotation angle for a nanoplatelet with slip ($k_e = 0.063$i) and without slip ($k_e = 0.028$). The red dashed line marks the asymptotic solution for σ^2 for purely imaginary values of k_e. The nanoplatelet has half-width $b = 0.25$ nm (i.e. $n = 1$) and half-length $a = 25$ nm. Region I: $Pe < Pe_I$, negligible slip effects for both $\lambda = 0$ and $\lambda = 2$ nm. Region II: $Pe_I \leq Pe < Pe_c$, moderate slip effects region characterised by changes in the frequency of rotation due to slip. Region III: $Pe \geq Pe_c$, large slip effects region where slip completely suppresses the rotation of the nanoplatelet.

$\lambda = 2$ nm (slip) for fixed $a/b = 100$ and $n = 1$. The corresponding effective aspect ratios are $k_e = 0.028$ and $k_e = 0.063$i for $\lambda = 0$ and $\lambda = 2$ nm, respectively. In figure 14, we plot the mean μ and variance σ^2 of the rotation angle for these two cases as a function of Pe. In agreement with figure 7, the results show that slip has no effect on particle orientation at low Pe, but has a strong influence on both μ and σ^2 at large Pe. To describe the qualitative differences in the trends of μ and σ^2 between the slip and no-slip cases, we subdivide the data into three different regions (I, II and III, see figure 14). Region III corresponds to $Pe > Pe_c$, where Pe_c is the critical value introduced in § 3.3 above which no full rotational cycles occur for $\lambda = 2$ nm. Region III is a 'large slip effects' regime. In this regime the platelet with slip performs small fluctuations around ϕ_c. In this region the curves approach smoothly the values expected for $Pe \to \infty$ (§ 3.2): for $\lambda = 2$ nm, μ is approximately constant ($\mu \approx |k_e|$), and $\sigma^2 \to 1/(2Pe|k_e|)$ as $Pe \to \infty$. This latter asymptotic solution for σ^2 can be obtained by inserting into (2.1) the linearisation of the angular velocity for angles close to ϕ_c, $\Omega = 2k_e(\phi - \phi_c)$ and assuming that p is Gaussian. For $\lambda = 0$, μ vanishes as $Pe \to \infty$ and σ^2 is finite, as predicted by Jeffery's theory. Regions I and II correspond to $Pe < Pe_c$. In region I, slip and no-slip curves for μ or σ^2 are practically indistinguishable, as apparently in this region the effect of the hydrodynamic stresses is subdominant with respect to Brownian stresses in setting the orientational dynamics. In region II, differences in the curves due to slip exists, but are not as marked as in region III. Region II corresponds to a 'moderate slip effects' regime, in which full rotational cycles occur even for platelets with an imaginary k_e, but with a significantly reduced frequency as compared with region I. This reduction in frequency indicates that in this region hydrodynamics mitigates the randomising effect of Brownian motion.

In regions II and III the effect of slip is to increase the mean and reduce the variance of the orientation distribution. The effect of slip on the variance is particularly evident: for

$Pe = 10\,000$, a small slip of $\lambda = 2$ nm leads to a reduction by approximately one order of magnitude of the variance.

As explained in § 3.2, the value Pe_I separating the 'negligible slip effects' regime and the 'moderate slip effects' regime must satisfy the condition $Pe_I \ll Pe_m = \min(|k_e^{-3}(\lambda = 0)|, k_e^{-3}(\lambda)|)$. Our numerical simulations (shown in both figures 7 and 14) indicate that the correlation $Pe_I \simeq 0.1 Pe_m$ provides a good approximation to the data for practical purposes.

In figure 15, we extend the analyses of figure 14 to assess the extent of the regions of large slip effects, moderate slip effects and negligible slip effects by evaluating Pe_c and Pe_I in the $(Pe, 2a)$ space. For our comparison, we use the same platelets and corresponding values of k_e used in figure 11. The difference to the analysis presented in § 3 is that now Pe_c and Pe_m can be evaluated as a function of the known variables λ and $2a$, rather than k_e.

We add to figure 15 red dash–dot lines corresponding to the Pe number for three shear stress values: $\dot{\gamma}\eta = 10^7$ Pa, $\dot{\gamma}\eta = 2 \times 10^4$ Pa, $\dot{\gamma}\eta = 10$ Pa (the Péclet number scales proportionally to the stress according to $Pe \approx c_1 \dot{\gamma}\eta a^3/(k_B T)$, where '$c_1 = 6.29 \pm 0.02$' was calculated from a boundary integral simulation of the hydrodynamic torque on a particle rotating with assigned velocity in a still fluid, see § 4.3). These characteristic shear stresses are, respectively, typical of: exfoliation processes in a low viscosity fluid (Paton *et al.* 2014); mixing in very viscous fluids (Huang & Terentjev 2012) and dispersion by microfluidisation (Karagiannidis *et al.* 2017; Paton *et al.* 2017); fast lubrication processes (Jonsson & Bhushan 1995), high-speed blade coating (Willenbacher, Hanciogullari & Wagner 1997) and MD simulations (Voeltzel *et al.* 2018; Gravelle *et al.* 2020; Gravelle, Kamal & Botto 2021). The effects of slip for each of these characteristic shear stresses can be assessed by identifying, for a given value of a, the region where the corresponding Pe lies. For example, the lowest shear stress (red dashed line in figure 15) is within the region where slip effects are negligible for all the values of λ, a and n we considered. For the intermediate shear stress (dotted–dashed line in figure 15) slip has a noticeable impact on the rotational dynamics: thicker platelets ($n = 10$) are likely to align if the slip length is sufficiently large so that k_e is purely imaginary. Otherwise for the thinner platelets, such as for $n = 1$, then there is a range of a and λ for which the average frequency for the platelets to complete a full rotational cycle is smaller than for a no-slip platelet. Finally, the highest shear stress (double-dotted–dashed line in figure 15) produces a value of Pe well within the 'large slip effects' region where the platelet fluctuates around ϕ_c if $\lambda > \lambda_c$.

The length of the platelet also affects the rotational dynamics. The local power law exponent characterising the dependence of Pe_c and Pe_I on a is smaller than 3 for comparatively small values of a ($a \ll 100$ nm approximately in figure 15), and approaches 3 as a increases. A consequence of the fact that the 'moderate slip effects region' is not bounded by parallel lines in a log–log plot is that for given particle thickness and shear stress value longer platelets are more likely to be affected by slip. Taking the case $n = 1$, $\lambda = 200$ nm, and $\eta\dot{\gamma} = 2 \times 10^4$ Pa as an example, the rotation of the platelet is not affected by slip for $2a < 40$ nm, whereas platelets with $2a > 40$ nm enter the 'moderate slip effects region' where slip effects start becoming significant.

4.5. *Effective viscosity of a dilute suspension of nanoplatelets with slip*

As an illustration of a macroscopic effect due to slip, in the current section we analyse the effects of stable alignment on the orientational contribution to the effective viscosity η_{eff} of a dilute suspension of nanoplatelets for finite values of λ. The effective shear viscosity

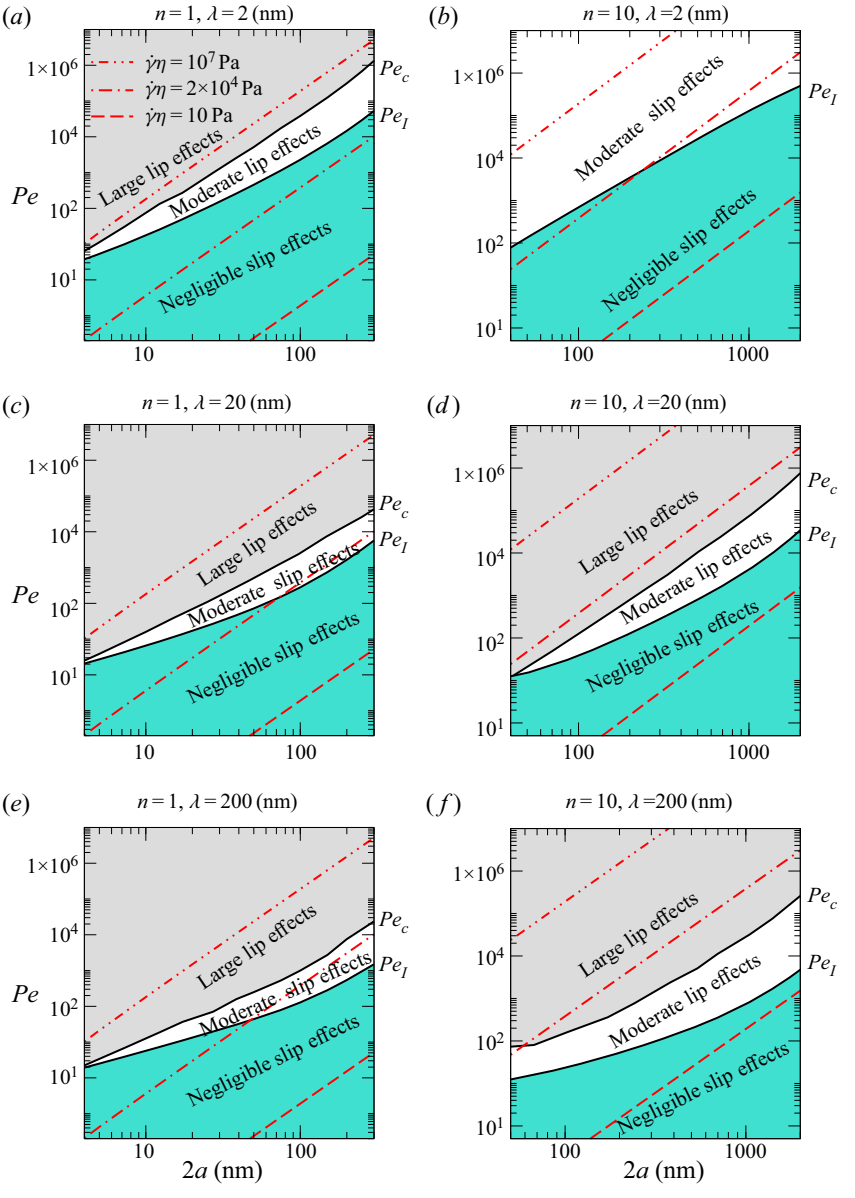

Figure 15. Effect of slip on the rotational dynamics of a nanoplatelet with length = depth = $2a$ and width = $2b$ in the (Pe, $2a$) space. Upper black curve marks the threshold Péclet number Pe_c for which $\sigma^2 = 2k_e$; above this threshold the hydrodynamic slip has a dramatic effect on the particle dynamics. Lower black curve marks the threshold Péclet number Pe_I; above this threshold, slip effects become important. The dashed, dashed–dot and dash–double-dot lines correspond to $\dot{\gamma}\eta = 10^7$ Pa, $\dot{\gamma}\eta = 2 \times 10^4$ Pa, $\dot{\gamma}\eta = 10$ Pa, respectively.

of a dilute suspension of particles can be calculated as

$$\eta_{eff} = \eta + \frac{\sigma'_{xy}}{\dot{\gamma}}, \tag{4.5}$$

where σ'_{xy} is the particle stress (Jeffery 1922; Giesekus 1962; Brenner 1974; Leal & Hinch 1971). For a suspension in which the motion of the particles is restricted to the flow plane,

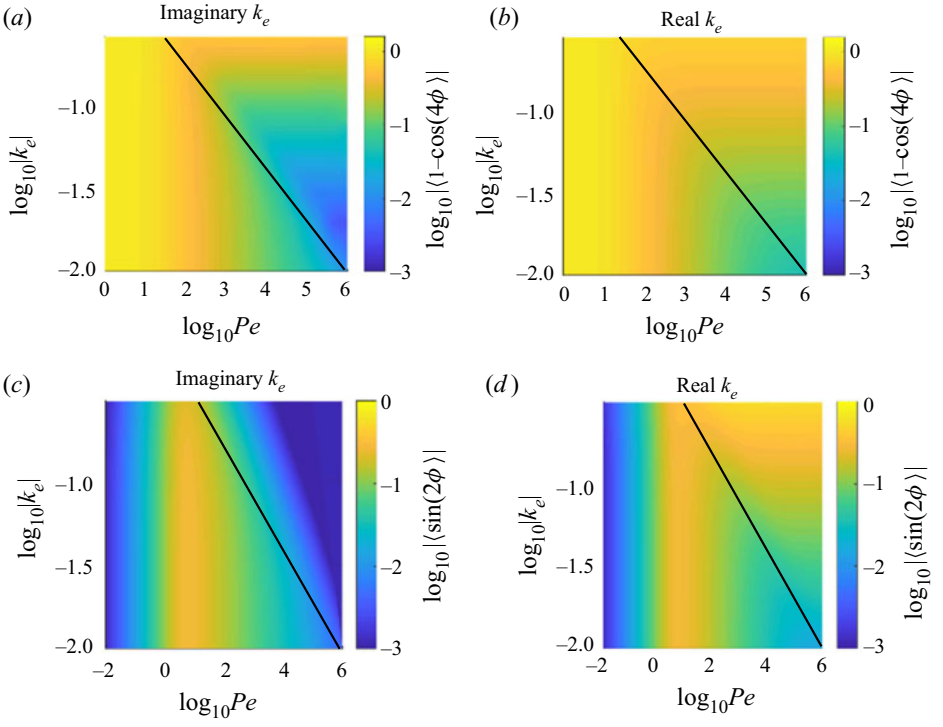

Figure 16. Colour maps of $\langle 1 - \cos(4\phi)\rangle$ and $\langle \sin(2\phi)\rangle$ in the (Pe, k_e) space for (a,c) an imaginary value of k_e and (b,d) a real value of k_e. The black line marks the equation $Pe = |k_e|^{-3}$.

to first order in the particle concentration, the particle stress can be written as

$$\sigma'_{xy} = c\eta\dot{\gamma}\left(\frac{A}{2}\langle 1 - \cos 4\phi\rangle + B + \frac{C}{2Pe}\langle \sin 2\phi\rangle\right), \tag{4.6}$$

where A, B and C are dimensionless coefficients (Rallison 1978) and c is the solid fraction. The first two terms on the right-hand side of (4.6) are due to the hydrodynamic stress acting on each platelet. The third term is the contribution of Brownian fluctuations to the particle stress.

As seen in § 3.2, slip has a strong influence on the time-averaged orientation of the particle, with consequences on the statistical quantities $\langle 1 - \cos 4\phi\rangle$ and $\langle \sin 2\phi\rangle$ in (4.6). A map quantifying how $\langle 1 - \cos 4\phi\rangle$ and $\langle \sin 2\phi\rangle$ vary in the (Pe, k_e) space is shown in figure 16. For $Pe \ll |k_e|^{-3}$, the quantities $\langle 1 - \cos 4\phi\rangle$ and $\langle \sin 2\phi\rangle$ are practically independent of whether k_e is real or purely imaginary. The term $\langle 1 - \cos 4\phi\rangle$ becomes significantly larger than $\langle \sin 2\phi\rangle$ for small Pe. Thus, the effective viscosity depends increasingly on $\langle 1 - \cos 4\phi\rangle$ as Pe decreases, in agreement with the theoretical results of Hinch & Leal (1972) and Leahy *et al.* (2015) (for elongated particles with $\lambda = 0$) and the experimental results of Del Giudice & Shen (2017) for graphene oxide.

For $Pe \gg |k_e|^{-3}$, hydrodynamic stresses become dominant. Figure 16 indeed reveals a strong dependency of $\langle 1 - \cos 4\phi\rangle$ and $\langle \sin 2\phi\rangle$ on k_e in this region. Since the prefactor of $\langle \sin 2\phi\rangle$ tends to zero for large Pe, here we focus on analysing the term $\langle 1 - \cos 4\phi\rangle$. The leading-order values of $\langle 1 - \cos 4\phi\rangle$ in this region can be estimated directly by using the

probability distributions calculated for $Pe \to \infty$ in § 3.2:

$$\langle 1 - \cos 4\phi \rangle = \begin{cases} 4k_e/(k_e+1)^2 & \text{if } k_e \in \mathbb{R}, \\ 1 - \cos 4\phi_c & \text{if } k_e \in i\mathbb{R}. \end{cases} \tag{4.7}$$

For $|k_e| \to 0$, $\langle 1 - \cos 4\phi \rangle$ tends to $4k_e$ and $8|k_e|^2$ for real or purely imaginary k_e, respectively. For $\lambda/a = 0$ and $\lambda/a \to \infty$, $\langle 1 - \cos 4\phi \rangle$ can be estimated in terms of the geometric aspect ratio k. For $\lambda = 0$, $k_e \propto k$, and so $\langle 1 - \cos 4\phi \rangle \propto k$. For $\lambda/a \to \infty$ we have $k_e \propto \mathrm{i}\sqrt{k}$, giving again $\langle 1 - \cos 4\phi \rangle \propto k$. Thus, quite interestingly, the limits $\lambda/a \to 0$ and $\lambda/a \to \infty$ yield a similar scaling relationship of $\langle 1 - \cos 4\phi \rangle$ with k.

For $\lambda = \lambda_c$, we have $k_e = 0$ and therefore $\langle 1 - \cos 4\phi \rangle = 0$. When $\langle 1 - \cos 4\phi \rangle$ vanishes, the particle stress reduces to $\sigma'_{xy} = c\eta\dot{\gamma}B$. If the variation of B on λ is sufficiently small in the neighbourhood of λ_c (compared with $A\langle 1 - \cos 4\phi \rangle$), then the value $\lambda = \lambda_c$ will correspond to a local minimum in the σ'_{xy} versus λ curve, because $A\langle 1 - \cos 4\phi \rangle \geq 0$ for all values of λ. Thus, the decrease in the value of σ'_{xy} with λ may not be always monotonic for large Pe.

5. Discussion

We have shown that the classical Bretherton's equation of motion can describe the rotational dynamics of thin rigid particles with surface slip, as long as an effective aspect ratio k_e is introduced to account for the hydrodynamic slip length λ in addition to the particle's shape. For a fixed geometric aspect ratio b/a and a small slip length $\lambda < b$ (with b the platelet's half-thickness), k_e is real, and an increase of λ simply leads to a decrease of k_e. However, when λ is sufficiently large in comparison with b, k_e becomes a purely imaginary number. In the limit of infinite Péclet numbers, a platelet with an imaginary k_e does not perform the periodic orbits predicted by the classical theory of Jeffery. Instead, the platelet's orientation fluctuates in time around a small angle ϕ_c with respect to the flow direction. We have identified a critical Péclet number Pe_c above which such stabilisation occurs, and below which rotations due to Brownian fluctuations appear. The numerical results suggest $Pe_c \sim 0.45|k_e|^{-3.4}$ for $|k_e| \ll 0.1$, and $Pe_c \sim 0.02|k_e|^{-4.8}$ for $|k_e| > 0.1$, with a smooth transition between the two scalings. An alternative critical Péclet number Pe_m, based on balancing the orders of magnitude of the convective and diffusive terms in (2.1), predicts the hydrodynamic stresses acting on the platelet to be dominant with respect to the Brownian stresses when $Pe_m = \min(|k_e^{-3}(\lambda = 0)|, k_e^{-3}(\lambda)|)$.

We find a negligible difference between the rotational behaviour of slip and no-slip platelets if Pe is smaller than $Pe_I \approx 0.1Pe_m$. In this regime, Brownian stresses dominate over hydrodynamic stresses in the regime where slip effects are important. For Pe smaller than Pe_c, Brownian fluctuations force the platelet with slip to complete full rotations, but with a period larger than the one expected in the no-slip case. Finally, we examined the effect of stable alignment on the orientational contribution to the effective viscosity by analysing how the term $\langle 1 - \cos 4\phi \rangle$ changes due to slip. At large Pe, we found that this term does not decrease monotonically with λ but instead attains a minimum value at $\lambda = \lambda_c$.

Some assumptions in our mathematical model require a discussion in view of the results. One aspect regards the rigidity of the particle, as thin particles are intuitively expected to be flexible. Assuming that the bending rigidity follows $B \sim Eb^3$ with E the Young's modulus (Poot & van der Zant 2008), where $E \sim 10^{11}$ Pa for pure graphene (Lindahl *et al.* 2012), for platelets aligned almost parallel to the direction of the shear

flow, buckling should occur when $\eta\dot{\gamma}(a/b)^2/E \geq 1$ (Lingard & Whitmore 1974; Kamal *et al.* 2020). Using the typical shear stress $\dot{\gamma}\eta \sim 10^4$ Pa for which slip effects become important (§ 4.4), one finds that the platelet behaves as rigid as long as the geometric aspect ratio $k \geq 10^{-7/2} \simeq 0.0003$. Therefore, the assumption of rigidity in our work may not be very restrictive for particles whose aspect ratio is not too extreme. Our results have been obtained for a 2-D geometry, which strictly speaking corresponds to a nanoplatelet with an infinite extent in the direction of the vorticity vector. Real nanoplatelets have, of course, a finite lateral size, with a shape that can vary considerably, from irregular 'pentagon' plate-shape (Del Giudice *et al.* 2018) to 2-D 'ribbon'-like (Hao *et al.* 2008)). However, it can be shown by comparing the hydrodynamic torque exerted on a 2-D plate-like particle with that on a 3-D disk that these different geometries lead to values of the effective aspect ratio k_e that are very similar to each other (Kamal *et al.* 2020). Therefore, the rotational dynamics is expected to be qualitatively similar for different plate-like objects, as long as the platelet's extent in the vorticity direction is not too small. Finally, a 3-D object also possesses extra degrees of freedom, i.e. its rotation is not confined to a plane. However, as discussed by Leahy *et al.* (2015) and Hinch & Leal (1972), the qualitative features of the rotational dynamics of a particle whose motion is confined to a plane are expected to be similar to those of a particle whose motion is in the full 3-D space. Therefore, we expect our model to have relevance to realistic systems. Additional insights would require the solution of full 3-D trajectories. MD results we have carried out with plate-like slip molecules rotating in the full 3-D space reveal that the 2-D approximation used here give rotational statistics that are comparable in trend and magnitude – with reasonably good approximation – to the ones computed from MD, giving us confidence in the value of the 2-D approximation employed here (Gravelle, Kamal & Botto 2021).

To illustrate how our theoretical results could be applied in practice, in § 4 we have considered geometric and slip parameters relevant to graphene and other 2-D nanomaterials. By calculating the values of Pe_m and Pe_c for typical values of k, b and λ, we have found that stresses $\dot{\gamma}\eta$ of the order of 10^4 Pa are required for hydrodynamic slip to affect quantitatively the rotational dynamics.

The use of fluid more viscous than water would allow for such large shear stress values. For instance, some ionic liquids have a viscosity approximately three orders of magnitude larger than that of water, while also showing slip length as large as 100 nm on graphene (Voeltzel *et al.* 2018). The use of very viscous fluids would have the further benefit of reducing the possibility of hydrodynamic instabilities and turbulences. Large viscous stresses may be accompanied by heating, but one could account for this effect by evaluating the viscosity and the slip length at the corresponding temperature.

An experimental verification of our results is not without challenges. For example, surface chemical modification of graphene nanoparticles is generally needed to obtain good dispersion of graphene in water, and when functionalisation is applied to the planar region of the platelet, the slip length is expected to be reduced (Wei, Peng & Xu 2014). Particles for which the functionalisation is limited to the particle edges may not have this problem (Park *et al.* 2017; Aliyeva *et al.* 2019), and could be more suitable to confirm the theory. Detecting rotation may not be trivial. For example, techniques that measure the average orientation of the particles may not enable one to clearly distinguish between a suspension in which very slender particles rotate but are oriented in a time-average sense, from a suspension in which the particle orientation angle is constant, since in both cases ϕ is expected to be small. Because the occurrence of a stable orientation depends only on the ratio λ/b, and not on the particle length, a solution could be to use plate-like particles that are thin ($b \sim 1$ nm) but not too long. For a given shear stress the ideal particle to

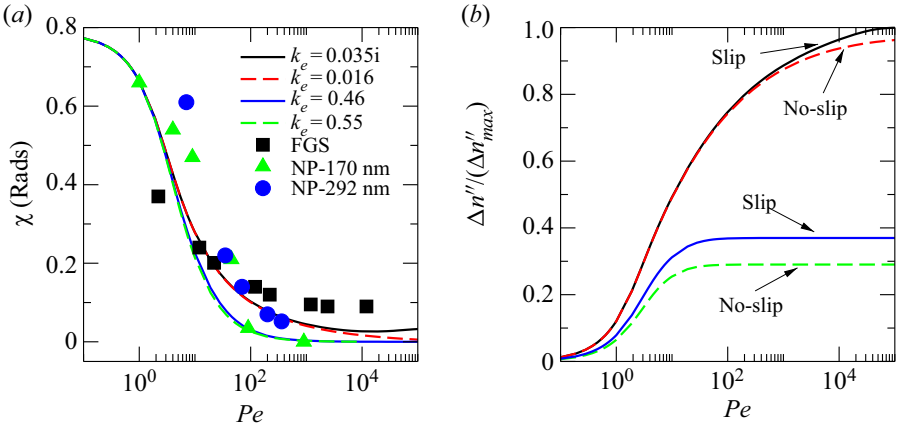

Figure 17. Comparison of our theory (for $\theta = \pi/2$) with experimental results of Reddy *et al.* (2018) for χ and $\Delta n''/\Delta n''_{max}$ (symbols), as defined in (5.1*a*,*b*). The different lines correspond to the following model parameters: functionalised graphene plateletes (FGS) with $k_e \approx 0.016$ (no-slip) and $k_e = 0.035$i (slip with $\lambda = 20$ nm); slightly oblate nanospheroids (NP) with $b/a = 0.55$, for $k_e \approx 0.55$ (no-slip) and $k_e \approx 0.46$ (slip with $\lambda/b = 0.21$).

evidence slip effects would be the shortest particle whose value of a is in the 'moderate slip effects' region, since this choice would give the largest variation in k_e due to slip, and thus the largest variation in ϕ. With this choice of particle length, the different rotational behaviours of slip and no-slip particles should be particularly evident.

In experiments, different statistical measures of particle orientation could be adopted, and some of them may be more sensitive to slip than others. To illustrate this dependence and the impact slip might have on orientational statistics that are evaluated in practice, we discuss two quantities that are usually measured in rheo-optical studies (Frattini & Fuller 1986; Fuller 1995; Vermant *et al.* 2001; Reddy *et al.* 2011): the average orientation angle χ and the degree of alignment $\Delta n''/(\Delta n''_{max})$, defined as

$$\chi = \frac{1}{2}\arctan\left(\frac{\langle \sin^2\theta \sin 2\phi\rangle}{\langle \sin^2\theta \cos 2\phi\rangle}\right), \quad \frac{\Delta n''}{\Delta n''_{max}} = \sqrt{\langle \sin^2\theta \sin 2\phi\rangle^2 + \langle \sin^2\theta \cos 2\phi\rangle^2}. \tag{5.1a,b}$$

Figure 17 compares our theoretical prediction for χ and $\Delta n''/(\Delta n''_{max})$ (in the case $\theta = \pi/2$) to the experimental data of Reddy *et al.* (2018). The experiments are for dilute polydisperse suspensions of functionalised graphene platelets, with average half-length $a = 250$ nm and half-thickness $b(n = 5) = 0.86$ nm, and slightly oblate gold nanospheroids, with $b/a = 0.55$ and lengths of either 170 nm or 290 nm. The functionalised graphene sheets were dispersed in mineral oil (viscosity $\eta = 100$ mPa s) and the oblate gold spheroids were dispersed in a glycerol/water mixture at 99.5 % glycerol ($\eta = 1.2$ Pa s). The theoretical values (lines) are for particles having the same average aspect ratio as in the experiments, and considering the limiting cases of $\lambda = 0$ and $\lambda = 20$ nm (figure 17). For large Pe, the functionalised graphene platelets where found experimentally to converge to a finite angle $\chi = 5^\circ$, instead of approaching 0 (as one would expect for a platelet with a no-slip boundary in the limit $Pe \to \infty$). The plot shows that our theory raises the $\chi - Pe$ curve closer to $\chi = 5^\circ$ at large Pe, although probably a value $\lambda = 20$ nm is larger than the one occurring in the experiment. Importantly, the plots show that for the slightly oblate spheroids, slight changes in k_e due to slip makes only a

slight change to χ (figure 17), but a more marked change in $\Delta n''/(\Delta n''_{max})$, suggesting that the second quantity is a more sensitive measure of slip effects.

We suggest that experiments similar to those of Reddy *et al.* (2018) could be done in which both χ and $\Delta n''/(\Delta n''_{max})$ are compared for a range of slip lengths and values of particle thickness. Rather than plotting χ or $\Delta n''/(\Delta n''_{max})$, one could also plot $\langle \sin^2\theta \sin 2\phi \rangle /2$ and $(2 - 2\langle \sin^2\theta \cos 2\phi \rangle - \langle \sin^2\theta \sin 2\phi \rangle^2)/4$. For small angles these quantities approximate the mean $\langle \phi \rangle$ and variance $\langle \phi^2 \rangle$, and should therefore have a marked variation in the neighbourhood of $\lambda/b = 1$ when plotted against λ/b. Another approach to evidence the effect of slip would be to conduct steady-state viscosity measurements (White *et al.* 2015; Del Giudice & Shen 2017), by focusing on the high-*Pe* regime where the effect of slip is maximum.

Our theory is not limited to nanometrically thin particles. Slip lengths of order 1 μm could be achieved for example, through the creation of a wetted/gas layer over the particle's surface (Lee, Charrault & Neto 2014), depletion layers (Tuinier & Taniguchi 2004; Fan, Dhont & Tuinier 2007) or surface nanobubbles (Neto *et al.* 2005; Yang *et al.* 2008). This raises the possibility of conducting experiments with relatively large plate-like particles whose dynamics can be accessed optically.

Applications of the theory developed in the current paper may include: (i) the development of rheological models for 2-D nanomaterials in suspension (e.g. graphene liquid crystals); (ii) the design of experimental methods to measure the slip properties of plate-like particles or macromolecules, which could yield insights into molecular interactions at the solid–liquid interface; (iii) the use of hydrodynamic slip to favour the flow of 2-D nanomaterials in narrow channel (e.g. to avoid clogging). Regarding (i), because we have shown that slip plate-like particles have a smaller propensity to rotate in shear flow than no-slip particles, and thus interactions with other particles are more limited than in the no-slip case, theories developed for the dilute case could also apply to more concentrated systems, as pointed out previously for ring-shaped particles (Singh *et al.* 2013; Borker *et al.* 2018). Finally, alignment is an essential ingredient to impart superior properties to nanocomposite materials. Surface modifications producing substantial slip could be used to align particles produced from the exfoliation of 2-D layered materials, which can be easily produced on mass scales by liquid-phase exfoliation (Botto 2019; Gravelle *et al.* 2020; Salussolia *et al.* 2020) and have therefore potential for applications. Because the ideal infinite Péclet number regime may not be achievable in practice, our results provide theoretical guidelines for deciding in which cases slip will have a dominant effect on the alignment of plate-like nanoparticles in the presence of Brownian motion.

Funding. This work was supported by the European Research Council (ERC) under the European Union's Horizon 2020 research and innovation program through project FlexNanoFlow (Grant agreement no. 715475).

Declaration of interests. The authors report no conflict of interest.

Author ORCIDs.
Catherine Kamal https://orcid.org/0000-0003-2813-0619;
Simon Gravelle https://orcid.org/0000-0003-2149-6706;
Lorenzo Botto https://orcid.org/0000-0002-7727-5155.

References

ALIYEVA, S., ALOSMANOV, R., BUNIYATZADEH, I., AZIZOV, A. & MAHARRAMOV, A. 2019 Recent developments in edge-selective functionalization of surface of graphite and derivatives–a review. *Soft Matt.* **17**, 448–466.

ALLISON, S.A. 1999 Low Reynolds number transport properties of axisymmetric particles employing stick and slip boundary conditions. *Macromolecules* **32**, 5304–5312.

ANCZUROWSKI, E. & MASON, S.G. 1967*a* The kinetics of flowing dispersions: II. Equilibrium orientations of rods and discs (theoretical). *J. Colloid Interface Sci.* **23**, 522–532.

ANCZUROWSKI, E. & MASON, S.G. 1967*b* The kinetics of flowing dispersions: III. Equilibrium orientations of rods and discs (experimental). *J. Colloid Interface Sci.* **23**, 533–546.

BOCQUET, L. & BARRAT, J.L. 2007 Flow boundary conditions from nano-to micro-scales. *Soft Matt.* **3**, 685–693.

BORKER, N.S., STROOCK, A.D. & KOCH, D.L. 2018 Controlling rotation and migration of rings in a simple shear flow through geometric modifications. *J. Fluid Mech.* **840**, 379–407.

BOTTO, L. 2019 Toward nanomechanical models of liquid-phase exfoliation of layered 2D nanomaterials: analysis of a $\pi-$peel model. *Front. Mater.* **6**, 302.

BRENNER, H. 1974 Rheology of a dilute suspension of axisymmetric Brownian particles. *Intl J. Multiphase Flow* **1**, 195–341.

BRETHERTON, F.P. 1962 The motion of rigid particles in a shear flow at low Reynolds number. *J. Fluid Mech.* **14**, 284–304.

BROWN, A.B.D, CLARKE, S.M., CONVERT, P. & RENNIE, A.R. 2000 Orientational order in concentrated dispersions of plate-like kaolinite particles under shear. *J. Rheol.* **44**, 221–233.

BURGERS, J.M. 1938 On the motion of small particles of elongated form suspended in a viscous liquid. *Kon. Ned. Akad. Wet. Verhand.(Eerste Sectie)* **16**, 113–184.

CHANG, Y.C. & KEH, H.J. 2012 Creeping-flow rotation of a slip spheroid about its axis of revolution. *Theor. Comput. Fluid Dyn.* **26** (1–4), 173–183.

CHUNG, D.D.L. 2002 Review graphite. *J. Mater. Sci.* **37**, 1475–1489.

COX, R.G. 1971 The motion of long slender bodies in a viscous fluid. Part 2. Shear flow. *J. Fluid Mech.* **45**, 625–657.

DEL GIUDICE, F., CUNNING, B.V., RUOFF, R.S. & SHEN, A.Q. 2018 Filling the gap between transient and steady shear rheology of aqueous graphene oxide dispersions. *Rheol. Acta* **57**, 293–306.

DEL GIUDICE, F. & SHEN, A.Q. 2017 Shear rheology of graphene oxide dispersions. *Curr. Opin. Chem. Engng* **16**, 23–30.

DOI, M. & EDWARDS, S.F. 1988 *The Theory of Polymer Dynamics*, International Series of Monographs on Physics, vol. 73. Oxford University Press.

FALK, K., SEDLMEIER, F., JOLY, L., NETZ, R.R. & BOCQUET, L. 2012 Ultralow liquid/solid friction in carbon nanotubes: comprehensive theory for alcohols, alkanes, OMCTS, and water. *Langmuir* **28**, 14261–14272.

FAN, T.H., DHONT, J.K.G. & TUINIER, R. 2007 Motion of a sphere through a polymer solution. *Phys. Rev.* E **75**, 011803.

FÉREC, J., HENICHE, M., HEUZEY, M.C., AUSIAS, G. & CARREAU, P.J. 2008 Numerical solution of the Fokker–Planck equation for fiber suspensions: application to the Folgar–Tucker–Lipscomb model. *J. Non-Newtonian Fluid Mech.* **155**, 20–29.

FRATTINI, P.L. & FULLER, G.G. 1986 Rheo-optical studies of the effect of weak Brownian rotations in sheared suspensions. *J. Fluid Mech.* **168**, 119–150.

FULLER, G.G. 1995 *Optical Rheometry of Complex Fluids*. Oxford University Press on Demand.

GARDINER, C. 2004 *Handbook of Stochastic Methods: For Physics, Chemistry & The Natural Sciences*. Synergetics, vol. 13. Springer.

GIESEKUS, H. 1962 Elasto-viskose Flüssigkeiten, für die in stationären Schichtströmungen sämtliche Normalspannungskomponenten verschieden groß sind. *Rheol. Acta* **2**, 50–62.

GRAVELLE, S., JOLY, L., YBERT, C. & BOCQUET, L. 2014 Large permeabilities of hourglass nanopores: from hydrodynamics to single file transport. *J. Chem. Phys.* **141**, 18–26.

GRAVELLE, S., KAMAL, C. & BOTTO, L. 2020 Liquid exfoliation of multilayer graphene in sheared solvents: A molecular dynamics investigation. *J. Chem. Phys.* **152** (10), 104701.

GRAVELLE, S., KAMAL, C. & BOTTO, L. 2021 Violations of Jeffery's theory in the dynamics of nanographene in shear flow. *Phys. Rev. Fluids* **6**, 034303.

HAO, R., QIAN, W., ZHANG, L. & HOU, Y. 2008 Aqueous dispersions of tcnq-anion-stabilized graphene sheets. *Chem. Commun.* **48**, 6576–6578.

HERZHAFT, B. & GUAZZELLI, É 1999 Experimental study of the sedimentation of dilute and semi-dilute suspensions of fibres. *J. Fluid Mech.* **384**, 133–158.

HINCH, E.J. & LEAL, L.G. 1972 The effect of Brownian motion on the rheological properties of a suspension of non-spherical particles. *J. Fluid Mech.* **52**, 683–712.

HINCH, E.J. & LEAL, L.G. 1973 Time-dependent shear flows of a suspension of particles with weak Brownian rotations. *J. Fluid Mech.* **57**, 753–767.

HUANG, Y.Y. & TERENTJEV, E.M. 2012 Dispersion of carbon nanotubes: mixing, sonication, stabilization, and composite properties. *Polymers* **4**, 275–295.

IVANOV, Y., VAN DE VEN, T.G.M. & MASON, S.G. 1982 Damped oscillations in the viscosity of suspensions of rigid rods. I. Monomodal suspensions. *J. Rheol.* **26**, 213–230.

JEFFERY, G.B. 1922 The motion of ellipsoidal particles immersed in a viscous fluid. *Proc. R. Soc. Lond.* A **102**, 161–179.

JOGUN, S.M. & ZUKOSKI, C.F. 1999 Rheology and microstructure of dense suspensions of plate-shaped colloidal particles. *J. Rheol.* **43** (4), 847–871.

JONSSON, U. & BHUSHAN, B. 1995 Measurement of rheological properties of ultrathin lubricant films at very high shear rates and near-ambient pressure. *J. Appl. Phys.* **78**, 3107.

KAMAL, C., GRAVELLE, S. & BOTTO, L. 2020 Hydrodynamic slip can align thin nanoplatelets in shear flow. *Nat. Commun.* **11**, 2425.

KANNAM, S.K., TODD, B.D., HANSEN, J.S. & DAIVIS, P.J. 2013 How fast does water flow in carbon nanotubes? *J. Chem. Phys.* **138**, 094701.

KARAGIANNIDIS, P.G., *et al.* 2017 Microfluidization of graphite and formulation of graphene-based conductive inks. *ACS Nano* **11**, 2742–2755.

KEH, H.J. & CHANG, Y.C. 2008 Slow motion of a slip spheroid along its axis of revolution. *Intl J. Multiphase Flow* **34** (8), 713–722.

KEH, H.J. & HUANG, C.H. 2004 Slow motion of axisymmetric slip particles along their axes of revolution. *Intl J. Engng Sci.* **42**, 1621–1644.

KELLER, S.R. & SKALAK, R. 1982 Motion of a tank-treading ellipsoidal particle in a shear flow. *J. Fluid Mech.* **120**, 27–47.

KIM, S. & KARRILA, S.J. 2013 *Microhydrodynamics: Principles and Selected Applications*. Courier Corporation.

KOLTONOW, A.R., LUO, C., LUO, J. & HUANG, J. 2017 Graphene oxide sheets in solvents: to crumple or not to crumple? *ACS Omega* **2**, 8005–8009.

KUMAR, A., SHARMA, K. & DIXIT, A.R. 2019 A review of the mechanical and thermal properties of graphene and its hybrid polymer nanocomposites for structural applications. *J. Mater. Sci.* **54**, 5992–6026.

LAUGA, E., BRENNER, M.P. & STONE, H.A. 2008 Microfluidics: the no-slip boundary condition. In *Springer Handbook of Experimental Fluid Mechnaics* (ed. C. Tropea, J.F. Foss & A. Yarin). p. 1219. Springer.

LEAHY, B.D., CHENG, X., ONG, D.C., LIDDELL-WATSON, C. & COHEN, I. 2013 Enhancing rotational diffusion using oscillatory shear. *Phys. Rev. Lett.* **110**, 228301.

LEAHY, B.D., KOCH, D.L. & COHEN, I. 2015 The effect of shear flow on the rotational diffusion of a single axisymmetric particle. *J. Fluid Mech.* **772**, 42–79.

LEAHY, B.D., KOCH, D.L. & COHEN, I. 2017 Controlling the alignment of rodlike colloidal particles with time-dependent shear flows. *J. Rheol.* **61**, 979–996.

LEAL, L.G. & HINCH, E.J. 1971 The effect of weak Brownian rotations on particles in shear flow. *J. Fluid Mech.* **46**, 685–703.

LEE, T., CHARRAULT, E. & NETO, C. 2014 Interfacial slip on rough, patterned and soft surfaces: A review of experiments and simulations. *Adv. Colloid Interface Sci.* **210**, 21–38.

LINDAHL, N., MIDTVEDT, D., SVENSSON, J., NERUSHEV, O.A., LINDVALL, N., ISACSSON, A. & CAMPBELL, E.E.B. 2012 Determination of the bending rigidity of graphene via electrostatic actuation of buckled membranes. *Nano Lett.* **12**, 3526–3531.

LINGARD, P.S. & WHITMORE, R.L. 1974 The deformation of disc-shaped particles by a shearing fluid with application to the red blood cell. *J. Colloid Interface Sci.* **49**, 119–127.

LOYALKA, S.K. & GRIFFIN, J.L. 1994 Rotation of non-spherical axi-symmetric particles in the slip regime. *J. Aerosol Sci.* **25**, 509–525.

LUAN, B. & ZHOU, R. 2016 Wettability and friction of water on a MoS2 nanosheet. *Appl. Phys. Lett.* **108**, 131601.

LUO, H. & POZRIKIDIS, C. 2008 Effect of surface slip on Stokes flow past a spherical particle in infinite fluid and near a plane wall. *J. Engng Maths* **62**, 1–21.

MAALI, A., COHEN-BOUHACINA, T. & KELLAY, H. 2008 Measurement of the slip length of water flow on graphite surface. *Appl. Phys. Lett.* **92**, 053101.

MUELLER, S., LLEWELLIN, E.W. & MADER, H.M. 2009 The rheology of suspensions of solid particles. *Proc. R. Soc.* A **466**, 1201–1228.

NETO, C., EVANS, D.R., BONACCURSO, E., BUTT, H.-J. & CRAIG, V.S.J. 2005 Boundary slip in Newtonian liquids: a review of experimental studies. *Rep. Prog. Phys.* **68**, 2859.

ORTIZ-YOUNG, D., CHIU, H.-C., KIM, S., VOÏTCHOVSKY, K. & RIEDO, E. 2013 The interplay between apparent viscosity and wettability in nanoconfined water. *Nat. Commun.* **4**, 2482.

PARK, J., KIM, Y.S., SUNG, S.J., KIM, T. & PARK, C.R. 2017 Highly dispersible edge-selectively oxidized graphene with improved electrical performance. *Nanoscale* **9**, 1699–1708.

PATON, K.R., ANDERSON, J., POLLARD, A.J. & SAINSBURY, T. 2017 Production of few-layer graphene by microfluidization. *Mater. Res. Express* **4**, 025604.

PATON, K.R., *et al.* 2014 Scalable production of large quantities of defect-free few-layer graphene by shear exfoliation in liquids. *Nat. Mater.* **13** (6), 624–630.

PETERLIN, A. 1938 Über die Viskosität von verdÜnnten Lösungen und Suspensionen in Abhängigkeit von der Teilchenform. *Z. Phys.* **111**, 232–263.

POOT, N. & VAN DER ZANT, H.S.J. 2008 Nanomechanical properties of few-layer graphene membranes. *Appl. Phys. Lett.* **92**, 063111.

POULIN, P., JALILI, R., NERI, W., NALLET, F., DIVOUX, T., COLIN, A., ABOUTALEBI, S.H., WALLACE, G. & ZAKRI, C. 2016 Superflexibility of graphene oxide. *Proc. Natl Acad. Sci.* **113**, 11088–11093.

POZRIKIDIS, C. 1992 *Boundary Integral and Singularity Methods for Linearized Viscous Flow*. Cambridge University Press.

POZRIKIDIS, C. 2002 *A Practical Guide to Boundary Element Methods with the Software Library BEMLIB*. CRC Press.

PRESS, W.H., TEUKOLSKY, S.A., VETTERLING, W.T. & FLANNERY, B.P. 2007 *Numerical Recipes 3rd Edition: The Art of Scientific Computing*. Cambridge University Press.

RADISAVLJEVIC, B., RADENOVIC, A., BRIVIO, J., GIACOMETTI, V. & KIS, A. 2011 Single-layer MoS2 transistors. *Nat. Nanotechnol.* **6**, 147–150.

RALLISON, J.M. 1978 The effects of Brownian rotations in a dilute suspension of rigid particles of arbitrary shape. *J. Fluid Mech.* **84**, 237–263.

REDDY, N.K., NATALE, G., PRUD'HOMME, R.K. & VERMANT, J. 2018 Rheo-optical analysis of functionalized graphene suspensions. *Langmuir* **34**, 7844–7851.

REDDY, N.K., PEREZ-JUSTE, J., PASTORIZA-SANTOS, I., LANG, P.R., DHONT, J.K.G., LIZ-MARZAN, L.M. & VERMANT, J. 2011 Flow dichroism as a reliable method to measure the hydrodynamic aspect ratio of gold nanoparticles. *ACS Nano* **5**, 4935–4944.

SADRON, C. 1953 *Flow Properties of Disperse Systems*. North-Holland.

SALUSSOLIA, G., BARBIERI, E., PUGNO, N.M. & BOTTO, L. 2020 Micromechanics of liquid-phase exfoliation of a layered 2d material: a hydrodynamic peeling model. *J. Mech. Phys. Solids* **134**, 103764.

SCHERAGA, H.A. 1955 Non-Newtonian viscosity of solutions of ellipsoidal particles. *J. Chem. Phys.* **23**, 1526.

SELLIER, A. 2012 Stokes flow about a slip arbitrary-shaped particle. *CMES* **87**, 157–176.

SELLIER, A. 2013 Arbitrary Stokes flow about a fixed or freely-suspended slip particle. *Comp. Model. Engng Comp.* **96**, 159–176.

SHERWOOD, J.D. & MEETEN, G.H. 1991 The use of the vane to measure the shear modulus of linear elastic solids. *J. Non-Newtonian Fluid Mech.* **41**, 101–118.

SHERWOOD, J.D. 2012 Resistance coefficients for Stokes flow around a disk with a Navier slip condition. *Phys. Fluids* **24**, 093103.

SILMORE, K.S., STRANO, M. & SWAN, J.W. 2021 Buckling, crumpling, and tumbling of semiflexible sheets in simple shear flow. *Soft Matt*.

SINGH, V., KOCH, D.L. & STROOCK, A.D. 2013 Rigid ring-shaped particles that align in simple shear flow. *J. Fluid Mech.* **722**, 121–158.

SINGH, V., KOCH, D.L., SUBRAMANIAN, G. & STROOCK, A.D. 2014 Rotational motion of a thin axisymmetric disk in a low Reynolds number linear flow. *Phys. Fluids* **26**, 033303.

STOVER, C.A., KOCH, D.L. & COHEN, C. 1992 Observations of fibre orientation in simple shear flow of semi-dilute suspensions. *J. Fluid Mech.* **238**, 277–296.

TAWARI, A.L., KOCH, D.L. & COHEN, C. 2001 Electrical double-layer effects on the Brownian diffusivity and aggregation rate of laponite clay particles. *J. Colloid Interface Sci.* **240**, 54–66.

TOCCI, G., JOLY, L. & MICHAELIDES, A. 2014 Friction of water on graphene and hexagonal boron nitride from *ab initio* methods: very different slippage despite very similar interface structures. *Nano Lett.* **14**, 6872–6877.

TUINIER, R. & TANIGUCHI, T. 2004 Polymer depletion-induced slip near an interface. *J. Phys-Condens. Mater.* **17**, L9.

VERMANT, J., YANG, H. & FULLER, G.G. 2001 Rheooptical determination of aspect ratio and polydispersity of nonspherical particles. *AICHE J.* **47**, 790–798.

VOELTZEL, N., FILLOT, N., VERGNE, P. & JOLY, L. 2018 Orders of magnitude changes in the friction of an Ionic liquid on carbonaceous surfaces. *J. Phys. Chem.* C **122**, 2145–2154.

WEI, N., PENG, X. & XU, Z. 2014 Breakdown of fast water transport in graphene oxides. *Phys. Rev.* E **89** (1), 012113.

WHITE, K.L., HAWKINS, S., MIYAMOTO, M., TAKAHARA, A. & SUE, H.-J. 2015 Effects of aspect ratio and concentration on rheology of epoxy suspensions containing model plate-like nanoparticles. *Phys. Fluids* **27**, 123306.

WICK, P., *et al.* 2014 Classification framework for graphene-based materials. *Angew. Chem. Int. Ed.* **53**, 7714–7718.

WILLENBACHER, N., HANCIOGULLARI, H. & WAGNER, H.G. 1997 High shear rheology of paper coating colors–more than just viscosity. *Chem. Engng Technol.* **20**, 557–563.

WILLIS, D.G. 1977 A kinematic model of preferred orientation. *Geol. Soc. Am. Bull.* **88**, 883–894.

XU, Y. & GREEN, M.J. 2014 Brownian dynamics simulations of nanosheet solutions under shear. *J. Chem. Phys.* **141**, 024905.

YANG, S., KOOIJ, E.S., POELSEMA, B., LOHSE, D. & ZANDVLIET, H.J.W. 2008 Correlation between geometry and nanobubble distribution on HOPG surface. *Europhys. Lett.* **81**, 64006.

YOUNGREN, G.K. & ACRIVOS, A. 1975 Rotational friction coefficients for ellipsoids and chemical molecules with the slip boundary condition. *J. Chem. Phys.* **63**, 3846–3848.

ZHANG, J., XU, X. & QIAN, T. 2015 Anisotropic particle in viscous shear flow: Navier slip, reciprocal symmetry, and Jeffery orbit. *Phys. Rev.* E **91**, 033016.